Manufacturing Q-optimized polymer-based mechanical resonators for cavity optomechanics with 3D direct laser writing

Daniel Stachanow

Masterarbeit in Physik
angefertigt im Institut für Angewandte Physik

vorgelegt der
Mathematisch-Naturwissenschaftlichen Fakultät
der
Rheinischen Friedrich-Wilhelms-Universität
Bonn

November 2024

I hereby declare that the work presented here was formulated by myself and that no sources or tools other than those cited were used.

Bonn, 19.11.2024 .....,
Date Signature

1. Supervisor: Prof. Dr. Sebastian Hoffetberth

2. Supervisor: Prof. Dr. Stefan Linden

Contents

CHAPTER 1

Introduction

Cavity optomechanics is a continuously advancing field of quantum physics, renowned for its ability to control mechanical oscillators through light-matter interaction down to the quantum level, as well as its applications in quantum sensing and technology [1]. In cavity optomechanics, the optomechanical coupling is enhanced by repeated light circulation, boosting the exerted radiation pressure of each individual photon [2]. This facilitates research on many fundamental and applied quantum mechanical research topics, such as ground-state cooling of macroscopic mechanical resonators [3], reaching the strong coupling regime for optomechanical systems [4], coherent frequency conversion [5], and quantum-limited sensing of forces and mass [6]. Its practical applications thereby benefit from the strong mechanical response of high-quality mechanical oscillators and the large optical readout sensitivity, that allow for high-precision sensing of a variety of physical quantities [6].

One way of realizing such systems is the "Membrane-In-the-Middle" (MIM) cavity, which was first demonstrated by Thompson et al. in 2008 [7]. Here, a cavity consisting of two stationary high-finesse mirrors is detuned by the oscillation of a thin dielectric membrane inside the cavity. This way, both the optical and mechanical components of the system are physically separated, which allows for independent optimization of each component.

Low optical losses and a high mechanical quality factor (Q-factor) are both important steps towards reaching the quantum regime in cavity optomechanics [8]. A high mechanical Q-factor, which corresponds to low energy dissipation, is also generally beneficial for larger sensitivity to forces and frequency shifts, and for less noise in most applications of optomechanical systems [9]. To achieve high Q-factors, state of the art experiments make use of the principle of dissipation dilution [10]. Here, the intrinsic material-dependent limits for the Q-factor are exceeded by inducing tensile strain in the oscillator material. In established systems, this is typically done with highly strained low-loss materials with good optical quality, such as silicon nitride [11].

Our Fiber Cavity Optomechanics (FCO) experiment in the Nonlinear Quantum Optics (NQO) group of Sebastian Hofferberth makes use of MIM cavities that combine the small mode volume of fiber Fabry-Pérot cavities with 3D direct laser written polymer oscillators. The fabrication method, done with the Nanoscribe, a commercial 3D direct laser writing system, in collaboration with the group of Stefan Linden, offers strong flexibility, enabling direct integration in a cavity system and favorable scaling towards 3D multi-mode mechanical structures. Recently, our group has successfully demonstrated such structures, focused on characterizing their optical and optomechanical performance [12]. However, a trade-off of the flexible fabrication method is that the mechanical Q-factor $Q \approx 20$ of

the fabricated membranes is strongly limited by the material properties of the used polymer resin. The overarching goal of this thesis is to increase this Q-factor by making use of dissipation dilution. For this, both the structure geometry and the fabrication process were revised and optimized, still maintaining its flexibility.
The structure of this thesis is the following. In Chapter 2, the theoretical fundamentals of optomechanics with fiber Fabry-Pérot cavities are introduced. Additionally, the testing process of fiber mirrors, which are built into our experimental setup, is demonstrated. In Chapter 3, the experimental setup, which, for this thesis, serves as a means of measuring the mechanical Q-factor of fabricated membranes through optomechanical coupling, is presented. The various dissipation channels, negatively impacting the mechanical Q-factor of our membranes, are discussed in Chapter 4. After calculations of the order of magnitude of each of the dissipation channel's contributions, the principle of dissipation dilution is derived, which is the basis for improving the Q-factor in this thesis. The fabrication process of the membranes with 3D direct laser writing is detailed in Chapter 5 and the optimization process of the fabrication to create dissipation-diluted mechanical oscillators is presented in Chapter 6.

CHAPTER 2

Fiber Fabry-Pérot Cavity Optomechanics

This chapter introduces the theoretical foundations of the experimental platform utilized for this thesis. Fiber Fabry-Pérot Cavity (FFPC) Optomechanics serves as both the application for the fabricated membranes and the characterizing method for evaluating their properties.
In Section 2.1, the working principle of cavity optomechanics is explained via the theoretical "mirror-on-a-spring" model. Here, the Hamiltonian, which describes the coupling of optomechanical interactions, is derived. Next, in Section 2.2, FFPCs are discussed, which are chosen as the optical platform for cavity optomechanics in our research group, as they enable the use of small and short cavities. The fabrication process of fiber mirrors and their properties within a cavity are discussed. Finally, in Section 2.3, the testing procedure, used for evaluating the properties of fiber mirrors, is outlined. A selection of fiber mirrors was tested before and after applying an annealing procedure, aimed at improving their quality. The fiber mirror with the highest optical quality is then selected for being built into the experimental setup, which is described in Chapter 3.

2.1 A brief introduction to Cavity Optomechanics

The fundamental model used to demonstrate the working principle of cavity optomechanics is the so-called "mirror-on-a-spring" cavity, illustrated schematically in Fig. 2.1. It is a simple way of visualizing the interaction between optics and mechanics in an optomechanical system. In this setup, one of the cavity mirrors is movable, as it is mounted to a wall via a spring, while the other remains stationary. When laser light is coupled into the cavity, the movable mirror is pushed back due to the radiation pressure from the photons of the laser beam. This mechanical displacement, in turn, alters the cavity length, which affects the light amplitude inside the cavity. Consequently, the radiation pressure exerted on the mirror is modified. This so-called "back-action" causes a closed loop between the optics and mechanics of such a system [13]. The following theoretical approach for discussing the underlying interaction is the Hamiltonian formulation, as introduced in [8].
Assuming single mode occupation, the uncoupled optical (ω_{cav}) and mechanical modes (Ω_m) can be described by two harmonic oscillators, leading to the free Hamiltonian

$$\hat{H}_0 = \hbar\omega_{\mathrm{cav}}\hat{a}^\dagger\hat{a} + \hbar\Omega_{\mathrm{m}}\hat{b}^\dagger\hat{b}\,. \tag{2.1}$$

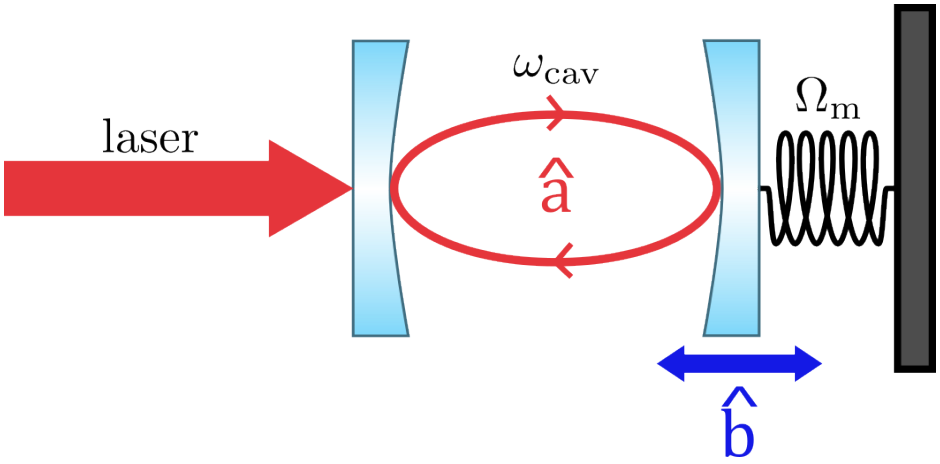

Figure 2.1: Schematic of the "mirror-on-a-spring" model, illustrating the principle of cavity optomechanics. The incoming laser beam couples into the cavity, where the laser light with resonance frequency ω_{cav} excites the optical mode $\hat{a}$. The radiation pressure of the photons of the laser beam pushes back the movable mirror, mounted via the spring, causing its oscillation with mechanical mode frequency Ω_{m}. The displacement of the mirror, depending on the phononic operator $\hat{b}$, results in a change of the cavity length. This leads to a so-called "back-action" on the optical mode and consequently to an optomechanical interaction loop.

Here $\hat{a}$, $\hat{a}^\dagger$ and $\hat{b}$, $\hat{b}^\dagger$ are the photonic and phononic annihilation and creation operators respectively. As the cavity resonance frequency ω_{cav} is dependent on the cavity length and, therefore, the displacement x of the movable mirror, one can expand it as

$$\omega_{\mathrm{cav}}(x) \approx \omega_{\mathrm{cav}} + x\frac{\partial \omega_{\mathrm{cav}}}{\partial x} + \cdots . \tag{2.2}$$

The linear coefficient $G = -\partial\omega_{\mathrm{cav}}/\partial x$, which is sufficient for describing most standard optomechanical systems, defines the optical frequency shift per displacement of the movable mirror. For a simple cavity, i.e. the "mirror-on-a-spring" cavity of length L, one can obtain $G = \omega_{\mathrm{cav}}/L$, meaning that smaller cavities introduce a more significant frequency shift per unit of displacement.
When expanding to the leading order in the displacement, one can express the Hamiltonian with Eq. (2.1) and Eq. (2.2) as

$$\hat{H} = \hbar\left(\omega_{\mathrm{cav}} - G\hat{x}\right)\hat{a}^\dagger\hat{a} + \hbar\Omega_{\mathrm{m}}\hat{b}^\dagger\hat{b}\,,$$

with the position operator $\hat{x} = x_{\mathrm{ZPF}}\left(\hat{b} + \hat{b}^\dagger\right)$. Here,

$$x_{\mathrm{ZPF}} = \sqrt{\frac{\hbar}{2m_{\mathrm{eff}}\Omega_{\mathrm{m}}}} \tag{2.3}$$

is the zero-point fluctuation, which is the fluctuation of the mechanical oscillator in its ground state around its equilibrium position. The effective mass m_{eff} of the mechanical resonator characterizes its response to displacements under applied forces.
By using Eq. (2.3) and defining the vacuum optomechanical coupling strength $g_0 = Gx_{\mathrm{ZPF}}$, the

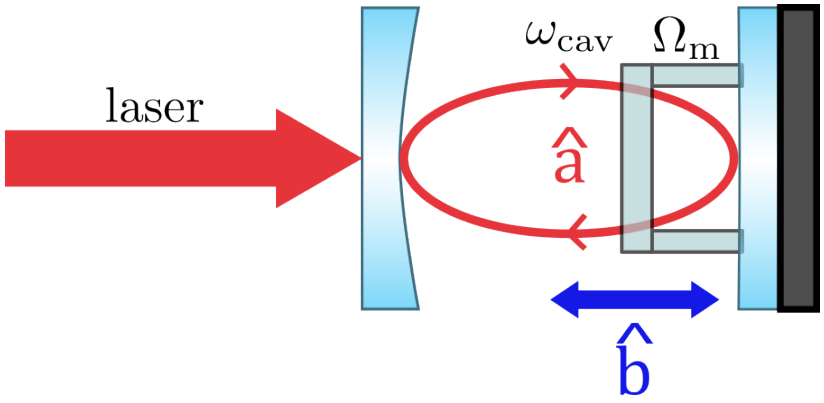

Figure 2.2: Schematic of a physically equivalent system to the "mirror-on-a-spring" model. An incoming laser beam couples into the cavity with resonance frequency ω_{cav}. The radiation pressure of the photons push back the membrane, which then oscillates with its mechanical mode frequency Ω_m. The resulting displacement of the membrane acts back on the optical mode, which creates an optomechanical interaction loop again.

interaction Hamiltonian can be expressed as

$$\hat{H}_{int} = -\hbar g_0 \hat{a}^\dagger \hat{a} \left(\hat{b} + \hat{b}^\dagger\right) .$$

Thus, the total Hamiltonian can be written as

$$\hat{H} = \hat{H}_0 + \hat{H}_{int} = \hbar\omega_{cav}\hat{a}^\dagger\hat{a} + \hbar\Omega_m\hat{b}^\dagger\hat{b} - \hbar g_0 \hat{a}^\dagger \hat{a} \left(\hat{b} + \hat{b}^\dagger\right) ,$$

where g_0 is the fundamental parameter describing the interaction strength between single photons and phonons.
The demonstrated Hamiltonian formulation is also applicable to other optomechanical systems, such as the membrane-in-the-middle (MIM) cavity, where both of the cavity mirrors are stationary and the oscillator is a semi-transparent membrane, placed inside the cavity [14]. This system, illustrated in Fig. 2.2, is used in this thesis. Here, one of the mirrors is a fiber mirror and the other is a plane mirror with fabricated membranes mounted on top. The experimental realization of this system is discussed in more detail in Section 3.1.
For a more in-depth look into optomechanics, especially the optomechanical coupling strength, please refer to Lukas Tenbrake's master thesis [15] from our experimental group.

2.2 Fiber Fabry-Pérot Cavities

The cavities used in our experimental system are hybrid Fiber Fabry-Pérot Cavities (FFPCs). Here, one of the cavity mirrors is a flat mirror substrate, while the other is a fiber mirror. After a brief description of the fabrication process of these fiber mirrors, their properties as part of a cavity and the advantages of a FFPC over a traditional cavity will be discussed.

2.2.1 Fiber mirror fabrication

The in-house technique for fabricating high quality fiber mirrors is via usage of a CO_2 laser shooting system to create controlled spherical depressions on cleaved fiber facets and then applying a reflective coating. In the following, this approach will be briefly discussed. For a more in-depth documentation refer to a thesis directly working with this setup [16].
The used high-power CO_2 laser operates at a wavelength of $\lambda = 9.3\,\mu\text{m}$, which aligns with the absorption peak of fused silica (SiO_2) [17], which is the base material of many optical fibers. Therefore, it is possible to strongly heat and, in turn, evaporate part of the fiber facet with the focused laser beam. As the laser has a Gaussian beam profile, this results in a near-spherical depression with radius $R \approx 200\,\mu\text{m}$. Due to the emerging surface tension, when the molten glass cools down, a very low surface roughness is achievable [18].
Next, the shot fiber facet is coated with alternating dielectric layers to achieve a Bragg-mirror surface with high reflectivity [14]. This is typically done by an external coating company (LAYERTEC or LASEROPTIK). As the laser used in the measuring setup of this thesis, which is further described in Section 3.1, has a wavelength of $\lambda = 780\,\text{nm}$, the coating is chosen so that the resulting fiber mirrors have reflectivities of up to 99.99 % around this wavelength.
Fiber-based cavities provide multiple benefits compared to traditional cavities [14]. Their compactness and open geometry in particular allow for easy adjustments of their position without the need for additional mode matching optics. They also allow for direct integration of membranes into high field concentration cavities with optical fibers.
This is needed for optomechanical experiments with small oscillators such as applied in this thesis.

2.2.2 Fiber Fabry-Pérot Cavity specifications

Following the discussion highlighting their importance, a brief overview of the properties of FFPCs is presented in the following. For a more general discussion on cavities and additional details on FFPCs, please refer to the thesis by Lukas Tenbrake from our experimental group [15].
The line shape of the cavity reflection signal contains essential information about the optical quality of the cavity and therefore, a physical description of the signal is required. A simple Lorentzian function is insufficient for this, as the spatial mode filtering of the reflected light results in a loss of light from the cavity [19]. This, among other effects, leads to an asymmetrical line shape, consisting of both a Lorentzian and a dispersive component

$$\frac{P_{\text{out}}(\nu)}{P_{\text{in}}} = \eta_r - \eta_{\mathscr{L}} \cdot \left(\frac{1}{1+\nu^2} - \mathscr{A} \frac{\nu}{1+\nu^2} \right), \tag{2.4}$$

with the normalized frequency detuning $\nu = 2\pi \left(\nu_{\text{laser}} - \nu_{\text{cav}} \right) / \kappa$, where κ is the linewidth. Here, η_r is the alignment-independent reflection amplitude for the off-resonant cavity and $\eta_{\mathscr{L}}$ is the Lorentzian

amplitude. The alignment- and geometry-dependent asymmetry parameter $\mathscr{A}$ represents the dispersive part of the signal [19].
After fitting a measured cavity reflection signal with the asymmetric Lorentzian above, one can extract two defining parameters, that characterize the quality of the fiber mirror. First, there is the so-called "Coupling Depth" (CD), which measures the fraction of light coupled into the cavity mode relative to the total input. It depends on factors such as the coupling efficiency [20]. Experimentally, the CD can be calculated as the ratio of the extinction of the cavity reflection signal at resonance frequency relative to the total light amplitude of the reflection signal off-resonance, given by [21]

$$\mathrm{CD} = \frac{P(\nu_{\text{off-res}}) - P(\nu_{\text{res}})}{P(\nu_{\text{off-res}})} \,. \tag{2.5}$$

The other relevant parameter is the finesse $\mathcal{F}$, which quantifies the cavity's ability to sustain light. It is mostly dependent on the reflection coefficient R and various losses, such as clipping losses, which are significant for cavity lengths of $L > 50\,\mu\mathrm{m}$, for the mirrors used in this thesis [22]. However, the cavities built in this thesis typically do not exceed this value. For negligible losses, one gets the well-known expression [23]

$$\mathcal{F} = \frac{\pi\sqrt{R}}{1-R} \,.$$

Alternatively, the finesse can be calculated from experimental values, as it directly impacts the temporal resolution of the reflection signal with

$$\mathcal{F} = \frac{\Delta_{\mathrm{FSR}}}{\Delta\nu_{1/2}} \,, \tag{2.6}$$

where $\Delta\nu_{1/2}$ is the full width at half maximum (FWHM) of two neighbouring dips of the reflection signal and Δ_{FSR} is the free spectral range, which quantifies their distance from one another [23].
The relevant quantities, that can be extracted from data, are illustrated in Fig. 2.5 in Section 2.3. Here, the shown coupling depth needs to be divided by the maximum light amplitude to obtain CD, as defined in Eq. (2.5).

2.3 Fiber mirror testing

For the used optomechanical system, discussed in Section 2.1, it is greatly beneficial to use a fiber mirror with a transmission tailored to the losses of the membrane inside the cavity, to achieve good impedance matching [15]. The previously used fiber mirror in the setup with a transmission of 2 000 ppm (0.2 %) is not sufficient for lossier structures than the ones used in previous experiments. Therefore, a large amount of previously manufactured fiber mirrors with a transmission of 6 000 ppm (0.6 %) were tested, to find a fiber mirror, which is best suited for integration into the experimental setup. Here, the finesse and coupling depth, when used in a cavity, are relevant. To further improve the optical quality of the tested fiber mirrors, experiments with annealing the fiber tips were made.

2.3.1 Testing procedure

Before being able to characterize a fiber mirror, one needs to couple laser light into its fiber. To do this, the other end of the fiber is first cleaved (cut) and then spliced (joined with another fiber) to a commercial single-mode fiber patch cable (Thorlabs P5-780Y-FC-1), using a fiber splicer (Fujikura 90S+). The used patch cables have a built-in fiber-coupler, making them easily integrable into an optical setup. The setup, that is used to evaluate the quality of a batch of manufactured 6 000 ppm fiber mirrors, is a simple testing setup, that is schematically illustrated in Fig. 2.3.
To measure the finesse and coupling depth, a cavity using the fiber mirror and a flat mirror substrate is built with an in-coupled 780 nm laser. Here, the fiber is mounted onto a movable 3D-stage with an integrated piezo. This allows for scanning the cavity length by moving the fiber mirror back and forth relative to the other mirror.

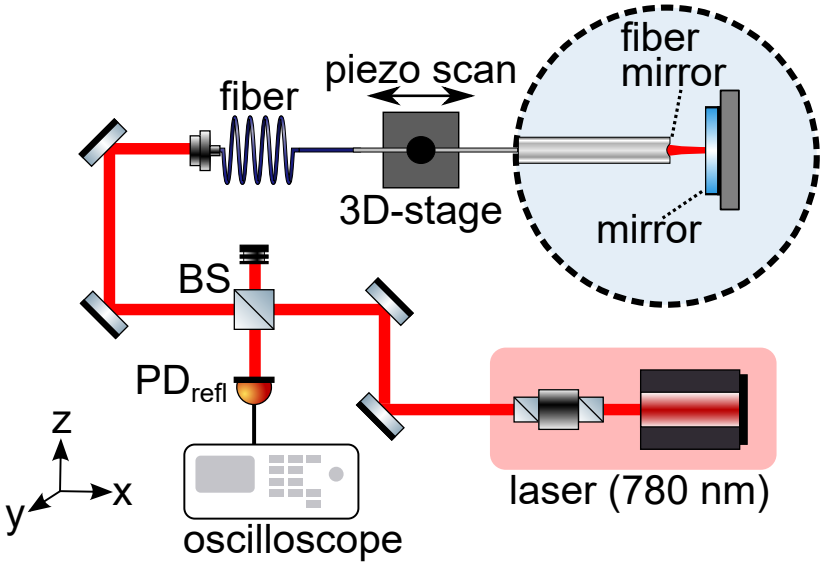

Figure 2.3: Schematic of the mirror testing setup, used to evaluate a fiber mirror's optical properties. A 780 nm laser is coupled into an optical fiber, that is spliced to a fiber mirror. A cavity is then built with the fiber mirror and a flat mirror substrate. To scan the cavity length, the fiber is mounted onto a 3D-translation stage with an in-built piezo. The back-reflection signal of the scanned cavity is then directed onto a photodiode and observed via an oscilloscope.

To observe a free spectral range, a piezo stage with sufficient travel range is employed. The FSR for a Fabry-Pérot cavity is given by $\Delta_{\mathrm{FSR}} = c/(2nL)$, where L is the cavity length, c is the speed of light and n is the refractive index of the medium inside the cavity ($n \approx 1$ for air) [24]. Using the resonance condition $L = m\lambda/2$, where λ is the wavelength of the laser and $m \geq 1$ is a positive integer [25], one can obtain that the cavity length must be shifted by at least

$$\Delta L = \frac{\lambda}{2} = \frac{780\,\mathrm{nm}}{2} = 0.39\,\mu\mathrm{m} \tag{2.7}$$

to observe one full FSR.
The back-reflection signal of the cavity is then coupled into free-space and guided onto a photo-diode ($\mathrm{PD}_{\mathrm{refl}}$) with a beam splitter (BS). The signal, measured by the photo-diode, is observed with an oscilloscope.
When testing a fiber mirror, the orientation of the large mirror substrate and fiber's position on the 3D-stage are adjusted manually, to optimize the alignment of the mirrors. The quality of alignment shows in the coupling depth and the presence of higher order modes, which are more pronounced for misaligned cavities. When the maximum coupling depth is reached via alignment, the cavity signal is recorded and fitted with a Lorentzian including a dispersion signal (see Eq. (2.4)). Using the fit parameters, the finesse (Eq. (2.6)) and coupling depth (Eq. (2.5)) can be calculated.

2.3.2 Annealing and final selection

Since all tested fiber mirrors showed lower optical quality than expected, a treatment of heating up the fiber tips was applied. This is beneficial because the thereby increased density of the glass can improve both the finesse and coupling depth [26].
To anneal the fibers, a simple setup, shown in Fig. 2.4, was built. Essentially, the fiber tips are heated up using a soldering iron. This is achieved by attaching a custom-made hollow cylindrical adapter to the soldering iron and carefully maneuvering the fiber tip inside it with a 3D-translation stage.
To determine feasible parameters for the temperature and duration of the process, tests with fiber mirrors with a low coupling depth and finesse were made, adjusting the parameters iteratively. A temperature of 300 °C has proven to be the most effective, as lower temperatures showed little to no effect. Therefore, the duration of the annealing process was varied for this fixed temperature. The applied annealing parameters and the resulting coupling depth and finesse in a cavity are detailed in Table 2.1. Additional attempts of annealing the fiber mirrors for durations $t \geq 30\,\mathrm{min}$ were made, but as most of these resulted in a complete loss of the reflection signal, they were excluded from the data. As demonstrated, a temperature of $T = 300\,^{\circ}\mathrm{C}$ combined with a duration of $t = 20\,\mathrm{min}$ yielded the most consistent improvements. Lower temperatures and shorter annealing times had less impact, while higher parameters frequently destroyed the fiber mirror entirely.
Therefore, these parameters were used to anneal the fiber mirror with the best optical quality found. This increased the coupling depth of the tested cavity to CD $\approx 90\%$ and the finesse to $F \approx 900$ for a laser wavelength of 780 nm. The measured full spectral range can be seen in Fig. 2.5 (a) and a zoom-in on the left cavity dip, that can be used to illustrate the coupling depth CD and FWHM, is shown in Fig. 2.5 (b).
The finesse increases even further for lower wavelengths but is sufficient for our used standard wavelength of 780 nm. This fiber mirror was then installed into the measurement setup, which is able to characterize the membranes fabricated in this thesis, as described in Section 3.2.

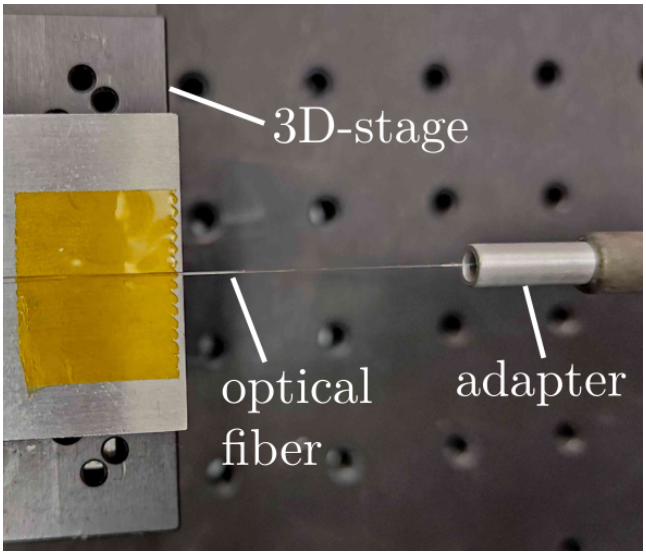

Figure 2.4: Image of the annealing procedure. The fiber is secured onto a 3D stage with Kapton tape and carefully inserted into a hollow, cylindrical adapter attached to a soldering iron. The temperature and duration of the process are adjusted iteratively.

Table 2.1: Comparison of coupling depth and finesse of multiple fiber mirrors before and after applying the annealing procedure for given durations at 300 °C. Fiber mirrors, which broke completely after the procedure, i.e. for durations of 30 min, and parameters with no effect, such as lower temperatures, are excluded.

Before		After		
Coupling Depth	Finesse	Coupling Depth	Finesse	Annealing duration at 300 °C,
> 80%	340	> 80%	435	15 min
> 75%	360	> 65%	500	20 min
> 50%	350	> 90%	460	20 min
> 60%	310	> 60%	270	20 min
> 30%	200	> 50%	350	20 min
> 80%	600	≈ 90%	> 900	20 min
> 60%	430	> 30%	140	30 min

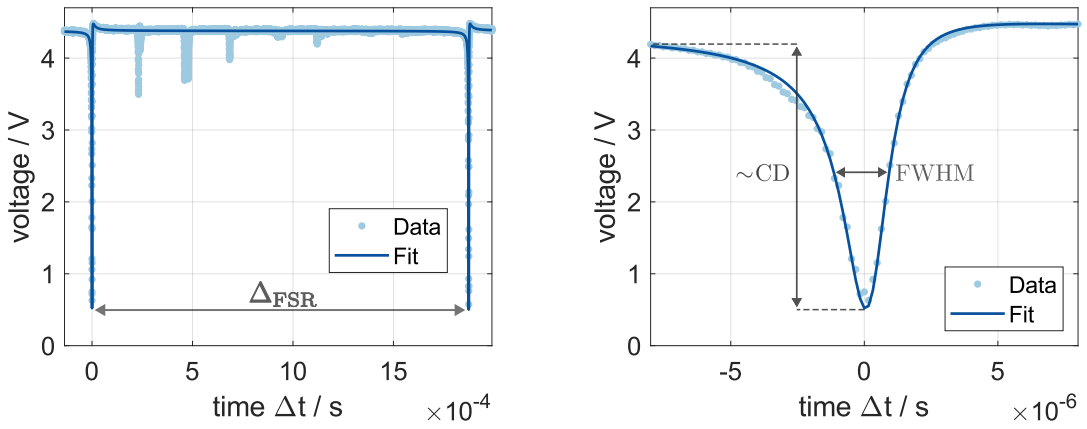

(a) (b)

Figure 2.5: Cavity reflection signal with fitted curve for the best fiber mirror after applying annealing procedure with resulting coupling depth CD $\approx$ 90% and finesse $F > 900$. One free spectral range Δ_{FSR} in **(a)** and a zoom-in on the first cavity dip in **(b)** are shown. Here, the approximate FWHM and CD are illustrated. To obtain the CD, as defined in Eq. (2.5), one needs to divide the shown CD by the maximum light amplitude of the photodiode signal.

CHAPTER 3

Measuring mechanical Q-factors with the Vacuum Fiber Microscope (VFM)

In the previous chapter, the properties and advantages of FFPCs for optomechanics were introduced. This chapter covers how FFPCs are used to characterize different fabricated membranes and in particular how their mechanical Q-factor is measured, which is a necessity for their optimization. To achieve this, the FFPCs are implemented with the Vacuum Fiber Microscope (VFM).
The VFM offers precise positioning of a fiber mirror in all spatial directions relative to the flat mirror surface, to which the membranes are attached to, effectively building a micrometer-scale cavity. By analyzing the cavity reflection signal through optics and electronics, information on the mechanical properties of the membranes can be gathered, as elaborated on in Section 3.1.
Furthermore, the process of upgrading the VFM with the second fiber mirror, which was presented in Section 2.3, is shown in Section 3.2. The addition of the holder with the second fiber mirror with higher transmission supports measuring the Q-factor of lossier structures. Therefore, building cavities with higher coupling depth is possible, which is beneficial for future measurements.

3.1 Operation of the VFM

The VFM is used as the primary experimental setup for optomechanics experiments in our research group. It utilizes the optical field of a laser to gather information about the micromechanical oscillators, which are fabricated in this thesis. The core of the VFM consists of a cavity with an integrated mechanical oscillator, as described theoretically in Section 2.1. One of the cavity mirrors is a stationary flat mirror substrate with a half-inch diameter, onto which multiple fabricated membranes can be mounted (discussed in the fabrication chapter, Chapter 5). The opposing mirror is a fiber mirror (see Section 2.2), with in-coupled laser light, which can be precisely positioned relative to the flat mirror using several translation stages. The cavity setup can be operated in ambient conditions, allowing for easy exchange of the flat mirror substrate, but it can also be placed inside a vacuum chamber and operated under vacuum pressure. For additional information as well as a description of the translation stage setup assembly, please refer to Florian Giefer's bachelor thesis [27] from our research group.
The optics and electronics setup of the VFM is illustrated schematically in Fig. 3.1 (a). A 780 nm wavelength laser, highlighted in red, is coupled into an optical fiber that is then fed through a vacuum chamber. Inside the chamber, the fiber is spliced to a fiber mirror, which is partially transmissive for

the in-coupled laser light. Together with a flat mirror substrate, onto which membranes are mounted, a cavity is formed. This is shown in Fig. 3.1 (b), where the small structures on the large blue mirror substrate are an array of membranes. The cavity length can be scanned using a shear-piezo, onto which the fiber is glued with an UV-cured epoxy, as depicted in Fig. 3.1 (c). By applying voltage to the piezo, the fiber and therefore the fiber mirror, is moved along the x-direction relative to the stationary mirror substrate. The fiber is guided through a ferrule to offer mechanical support, which, in turn, reduces the optical cavity noise, induced by the scanning of the fiber position. The substrate itself can also be moved in the y-z-plane with translation stages and be rotated with a rotation stage. Moving the substrate flexibly allows scanning across multiple structures. This is why arrays of membranes with varying properties are typically fabricated onto one mirror substrate, as shown in Fig. 3.1 (b). Observing how the FFPC's properties depend on the position of the substrate, gives insight into the membrane properties.

The back-reflected cavity signal is coupled back into the optical fiber and directed into the free-space part of the setup. Here, a beam splitter (BS) guides the light onto a photodiode PD_{refl}. The recorded signal typically shows an intensity dip at the cavity's resonance frequency ν_0, as depicted in Fig. 2.5 in the previous chapter. However, this frequency is slightly shifting back and forth over time by an amount $\Delta\nu$. This is indicated in the cavity signal shown in Fig. 3.1 (a).

This frequency noise originates from thermal occupation of vibrational modes of the membrane at room temperature, which influences the resonance frequency of the cavity. As a result, the optical signal provides information on the properties of the mechanical oscillator. For a more in-depth discussion of this effect, please refer to Lukas Tenbrake's master thesis from our research group [15]. Since the thermal noise is relatively weak compared to other noise sources in the experiment, a locking scheme is applied to filter out the unwanted noise.

The locking scheme applied here is side-of-fringe locking [28]. A constant offset is added to the input signal, creating two zero-crossings on the sides of the cavity dip. The sides of the dip are now set as reference points. In case of a decreasing frequency of the measured signal relative to the set point, the signal will turn negative and for an increasing frequency the signal becomes positive. This generates an error signal, which is fed into a proportional-integral (P-I) controller to compensate for frequency noise in the cavity. However, as the typical eigenfrequencies of the fundamental mode of the fabricated membranes exceed the maximum locking bandwidth ($\sim 100\,\mathrm{kHz}$), the noise caused by the membranes is still present in the stabilized signal. Therefore, the signal can be analyzed using an Electrical-Spectrum-Analyzer (ESA).

This is illustrated schematically in Fig. 3.2. Due to the oscillation of the membrane, the resonance frequency of the cavity dip is slightly modulated over time with a frequency shift $\Delta\nu$, as depicted in red. This leads to a periodic shift of the amplitude ΔA, shown in purple, at the locked cavity frequency point (blue). When this signal is fed into the ESA, the ESA decomposes the noise into its frequency components, which results in a Lorentzian distribution in frequency space, centered around the resonance frequency of the membrane. The Full Width at Half Maximum (FWHM) of this peak contains information on the damping of the oscillation and consequently, the mechanical Q-factor of the membrane. An in-depth discussion of the Q-factor and the various damping mechanisms affecting it can be found in the following chapter, Chapter 4.

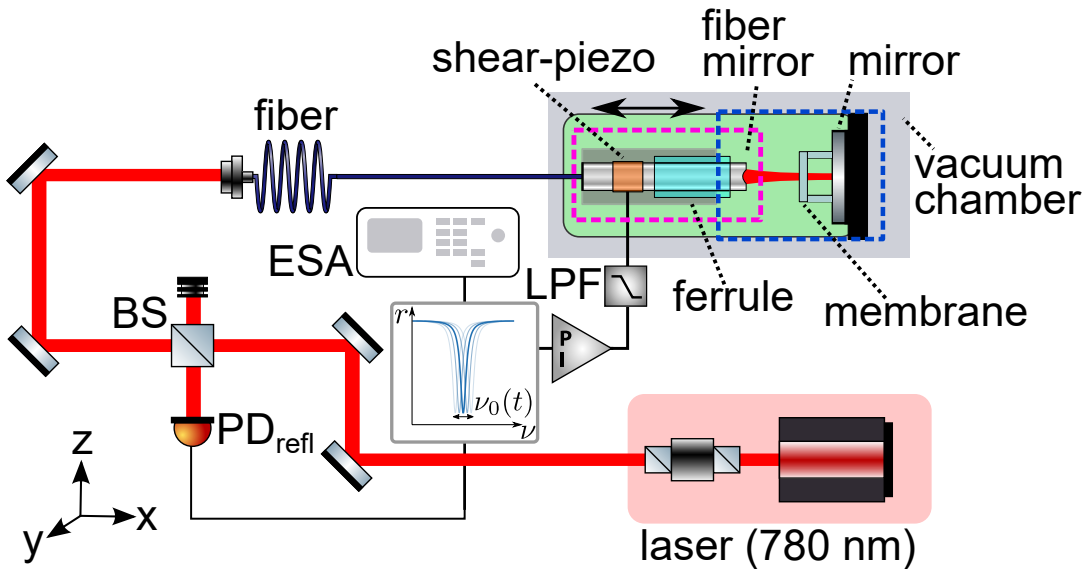

(a)

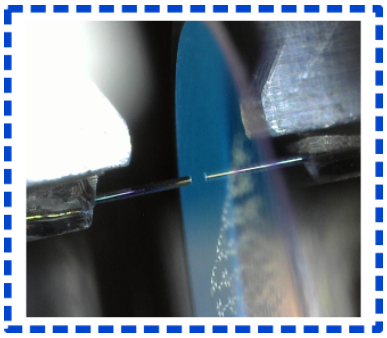

(b)

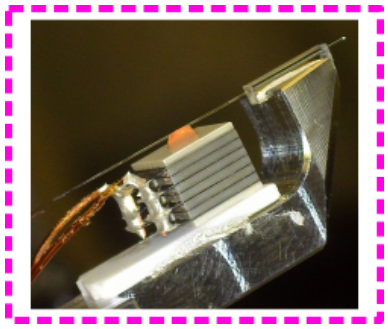

(c)

Figure 3.1: **(a)** Schematic of the Vacuum Fiber Microscope (VFM) setup. The light of a 780 nm laser (highlighted in red) is coupled into an optical fiber. The fiber is spliced to a fiber mirror, which is fed through a vacuum chamber, where it is stabilized mechanically by a ferrule. Together with a flat mirror substrate with fabricated membranes mounted on top, the fiber mirror is part of an optical cavity. This can also be seen in **(b)**, where an array of multiple membranes is mounted on top of the blue mirror substrate, that faces the fiber mirror. The substrate can be moved in the y-z-plane with translation stages and rotated with a rotation stage. The cavity length can additionally be scanned in the x-direction via a shear-piezo, that the fiber is connected to, shown in **(c)**. The reflection signal of this cavity is coupled back into the free-space part of the setup. Here, a beam splitter (BS) guides the light onto a photodiode PD_{refl}. The recorded signal is then locked via the side-of-fringe method to stabilize the cavity via a P-I-controller and also given to an ESA, which transforms the un-filtered cavity noise, originating from the membrane, into frequency space.

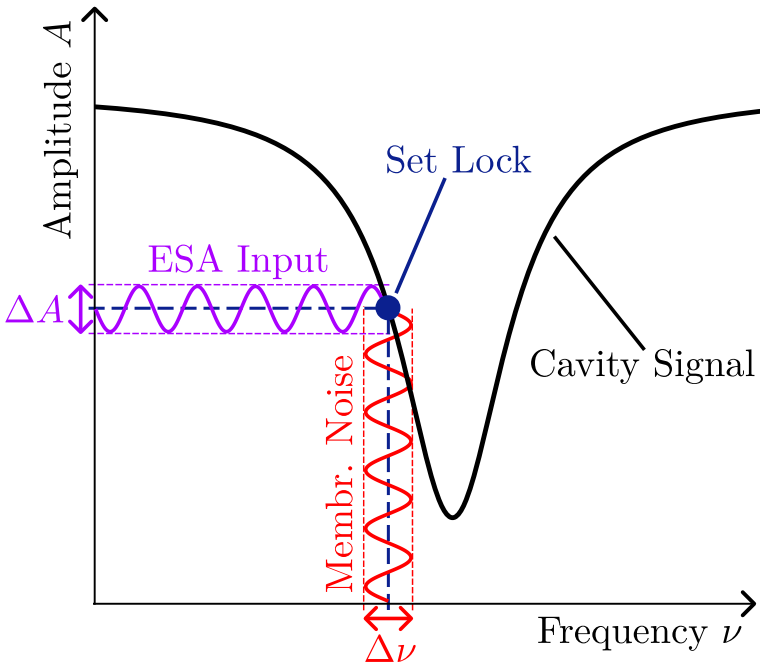

Figure 3.2: Schematic of the frequency noise caused by the oscillation of the membrane inside the cavity. The cavity signal is slightly modulated in its resonance frequency (red), which leads to an oscillation of the amplitude (purple) at the set locked frequency (blue). This amplitude fluctuation at the frequency of the mechanical oscillator's eigenfrequency acts as an input signal for an ESA, which transforms the noise into frequency space. The resulting signal contains information on the mechanical Q-factor of the membrane.

3.2 Upgrading the VFM

As of the start of working on this thesis, only a single fiber mirror was installed in the VFM. Due to its low transmission of 2 000 ppm (0.2 %), the impedance matching with lossier membrane structures than previously fabricated [15] is suboptimal, as discussed in Section 2.3. Additionally, cavities built with this fiber mirror achieved a maximum coupling depth of only about 60%. Given the parameters of the 6 000 ppm transmission fiber mirror, which in the testing process showed a finesse of $F > 900$ and a coupling depth of CD $\approx 90\%$, a second holder for the additional fiber was integrated into the setup. This was easily achievable as the original design of the setup was already made with two fiber mirrors in mind [27]. After the preparation and installation of the holder, the fiber mirror was tested once more by building a cavity.

3.2.1 Building the fiber mirror holder

The holder, fabricated from aluminum in our institute's mechanics workshop, is shown in Fig. 3.3. The originally planned design for the second fiber mirror holder [27] was taken and only slightly adjusted. To accurately measure the optical quality of fabricated membranes, one needs to scan across multiple free spectral ranges (FSRs) of the cavity to make consistent finesse measurements. As calculated in Eq. (2.7), a travel range of at least 0.39 µm is needed to measure one FSR.
Initial tests with a lower-quality fiber mirror indicated that the travel range of the originally selected piezo (PL5FBP3 from Thorlabs) was insufficient. The specified travel range of 1.3 µm was not reached, possibly due to friction between the fiber and the holder. To ensure a sufficient travel range, a piezo stack (P-111.03T from Physik Instrumente) with a specified range of 3 µm was chosen instead. Due to the increased height of this piezo stack, the designated part of the holder for its attachment was lowered, compared to the previous design for the other piezo.

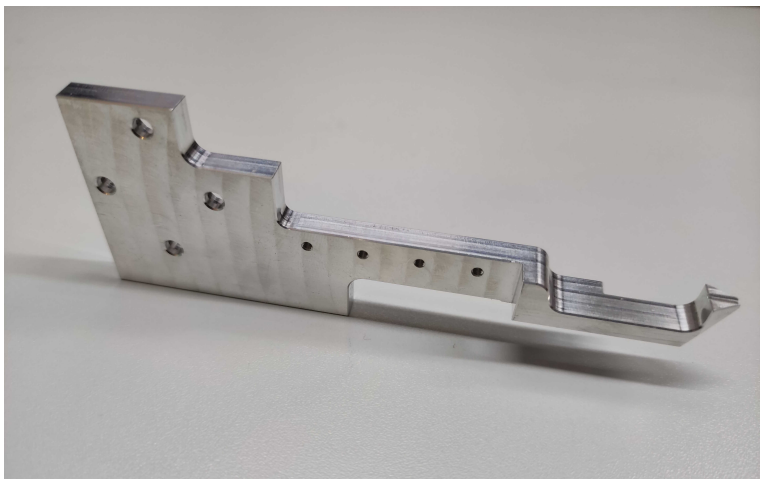

Figure 3.3: Second fiber mirror holder for the VFM setup, fabricated in our institute's mechanics workshop out of aluminum. The large holes are designed for mounting the holder onto a translation stage, while the smaller holes are intended for attaching an actuator, which stabilizes cavities built with the setup. The geometry was slightly altered from the original design to account for a new piezo stack used, to be able to observe additional free spectral ranges.

To assemble the holder, both the piezo and the stabilizing ferrule (a glass ferrule from VitroCom) were glued onto the holder, as shown in Fig. 3.4. All of the components are glued together with conductive two-component silver epoxy (H20E by EPO-TEK), which allows for voltage supply to the piezo, when attaching wires to its contacts. To harden the glue, it requires heat curing in an oven at about 150 °C for one hour. To prevent short circuits between the piezo and the aluminum holder, a non-conductive ceramics plate is glued onto the holder as an insulating layer. The piezo stack is then glued on top of the ceramics plate, with two coated copper wires threaded through each of the piezo contacts.
Next, the fiber mirror needs to be carefully guided through the ferrule, for which a precise positioning setup is required, that is depicted in Fig. 3.5. The holder is clamped onto an aluminum block, mounted onto a 1D-translation stage. Due to the geometry of the holder, the fiber must be inserted into the ferrule from the top. To achieve this, the fiber is attached to a rod construction using Kapton tape. The rod construction is mounted to a motorized 2D-translation stage, enabling 3D movement in combination with the other stage. To carefully insert the fiber into the transparent ferrule, two USB microscopes are used to closely examine the ferrule opening as well as the inside of the ferrule channel. After successful insertion of the fiber, it is glued onto the piezo stack with UV-epoxy, which hardens upon exposure to UV light, leading to an orange color, as can be seen in Fig. 3.4. Finally, the Kapton tape securing the fiber to the rod is removed by applying isopropyl alcohol (IPA) to dissolve the glue of the tape.

3.2.2 Final testing

After successful preparation of the holder, it was tested by building a cavity with a flat mirror. Here, the reflection signal was monitored while scanning the cavity with the piezo stack's maximum travel range. As depicted in Fig. 3.6 (a), multiple free spectral ranges were now observed, as expected. However,

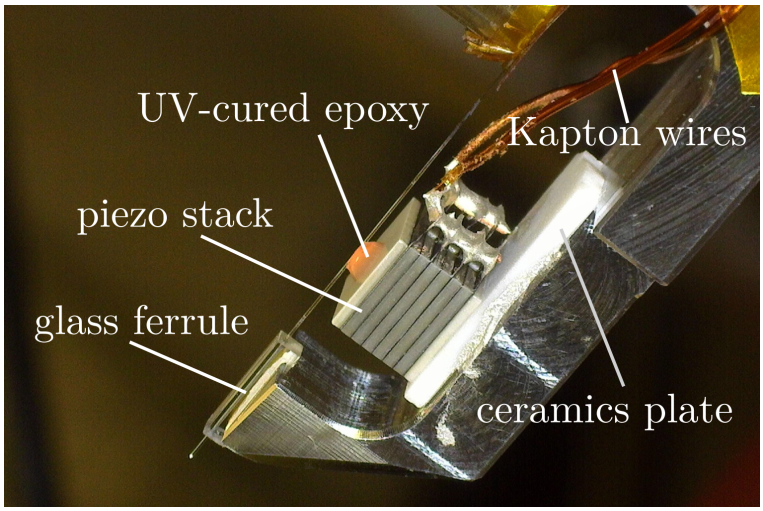

Figure 3.4: Assembled fiber mirror holder. All of the parts are glued together with silver glue. The piezo stack, with Kapton wires connected to its contacts, is glued onto the holder with an insulating ceramics plate inbetween to prevent short circuits. The fiber is then threaded through a glued-on glass ferrule and lastly attached to the piezo stack with UV-curable epoxy.

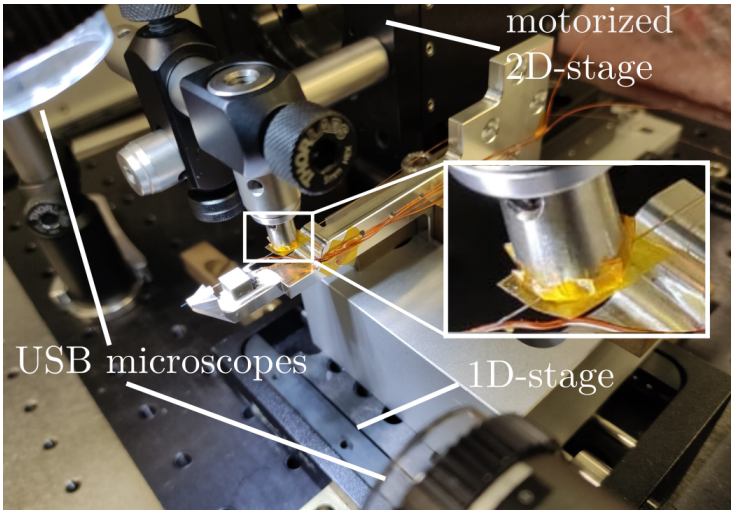

Figure 3.5: Fiber insertion setup for the VFM holder. The holder is clamped onto an aluminum block, which is attached to a 1D-stage. The fiber is secured on a rod construction, that is movable via a motorized 2D-stage, with Kapton tape (see zoom). To make the insertion process easier, two USB-microscopes are used for visual inspection.

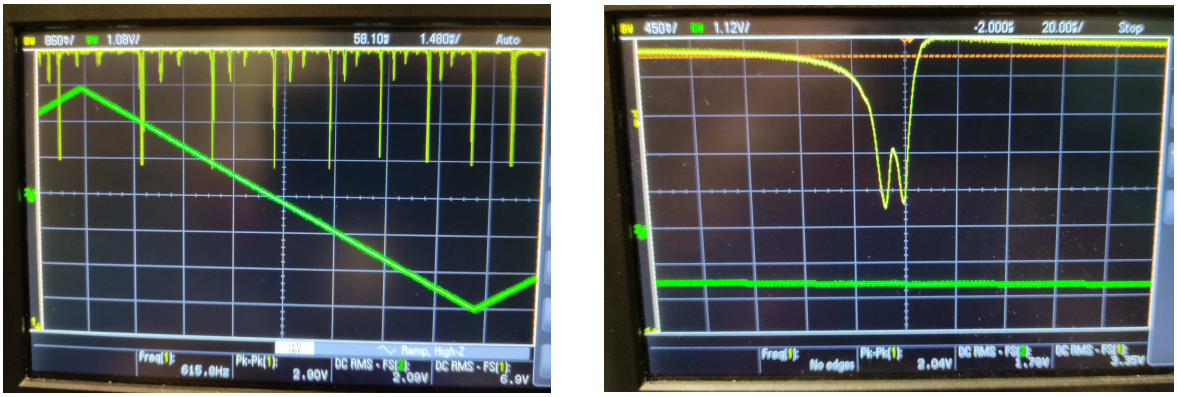

(a) (b)

Figure 3.6: Reflection signal of a cavity built with the new fiber mirror (yellow) after installing it into the holder and applying a voltage ramp (green) onto the piezo stack. **(a)** Various free spectral ranges are within the scan range of the new piezo stack. However, the coupling depth is significantly lower than for previous tests in Section 2.3. **(b)** This is due to a splitting the mode, resulting from polarization effects.

the coupling depth was greatly reduced compared to the previous measurements in Section 2.3. After further alignment optimization, which did not lead to significant improvements, a closer inspection of one of the reflection dips, shown in Fig. 3.6 (b), revealed a douple-dip rather than a single mode. Further testing indicated that this splitting was caused by polarization effects. When adjusting the polarization of the light inside the fiber using a manual fiber polarization controller (FPC030 by Thorlabs), the reflection signal returned its previously measured shape in Section 2.3. This polarization effect likely was caused by an elliptical shot of the fiber mirror [22], which needs to be compensated for before doing measurements.

Finally, the holder with the second fiber mirror was installed into the VFM setup, as depicted in Fig. 3.7. It is mounted to one of the various translation stages, moving the holders and the mirror substrate holder. To increase the mechanical stability of built cavities, an actuator was added to the holder, which can establish physical contact to the flat mirror substrate holder. This prevents the mirrors from moving relative to one another due to mechanical vibrations of the setup.
As previously mentioned, the depicted VFM setup can be placed into a vacuum chamber, which is an important feature for quantifying the mechanical quality of the fabricated membranes. This is due to gas damping losses at ambient pressures, that are one of the significant mechanical dissipation channels, which influence the mechanical Q-factor of micromechanical resonators [29]. The various loss channels and additional ways to combat them for our structures are further discussed in the following Chapter 4.

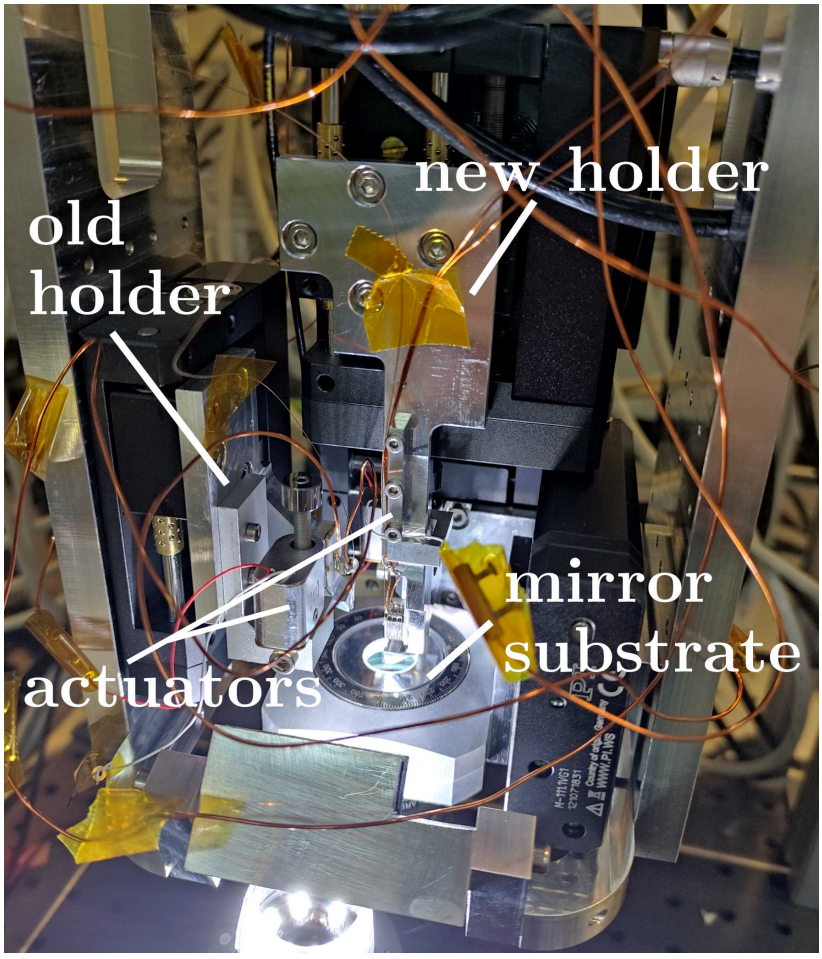

Figure 3.7: VFM setup with the installed second fiber mirror holder in use. The holder is mounted onto a translation stage. To mechanically stabilize the cavity, an actuator was installed, that establishes physical contact between the fiber mirror holder and the mirror substrate holder.

CHAPTER 4

Dissipation Dilution in micromechanical oscillators

The mechanical quality factor (Q-factor) of the fabricated membranes, which will be optimized in this thesis, quantifies the performance of their oscillations. This chapter introduces the Q-factor and analyzes the factors that influence it.
First, the Q-factor is defined and the various loss mechanisms affecting micromechanical oscillators are reviewed in Section 4.1. Some developed techniques for reducing these losses are also briefly covered.
Next, in Section 4.2, estimations of the order of magnitude for the Q-factor of each loss mechanism are presented.
Finally, the principle of dissipation dilution is introduced in Section 4.3. Dissipation dilution refers to applying a constant external potential to the oscillator to suppress its intrinsic material losses. This technique will play an essential role for improving the Q-factor in the fabrication process, as discussed in the following chapter, Chapter 5.

4.1 Mechanical loss mechanisms

The Q-factor is an important measure to describe the rate of energy loss of a resonator. Its most common definitions are the bandwidth definition and the stored energy definition.
The bandwidth definition [30], is given by

$$Q = \frac{f_0}{\Delta f},$$

where f_0 is the resonance frequency and Δf is the resonance width, is commonly used for quantifying the Q-factor from experimental data. As discussed in Section 3.1, the measurement setup used in this thesis produces a Lorentzian curve, that characterizes the oscillation around the membrane's resonance frequency. Here, one can easily determine both f_0 from the center frequency and Δf from the FWHM of a Lorentzian fit.

The stored energy definition [30]

$$Q = 2\pi \cdot \frac{\text{energy stored}}{\text{energy dissipated per cycle}} = 2\pi \cdot \frac{W}{\Delta W} \tag{4.1}$$

provides a more intuitive way of understanding the Q-factor. Here, the Q-factor is increased by the stored energy in the oscillator and decreased by the energy dissipated per oscillation cycle. There are various energy dissipation channels, which will be discussed in the following. The overall Q-factor is given by the sum of the inverse of all the dissipation mechanisms as [29]

$$\frac{1}{Q} = \frac{1}{Q_{\text{medium}}} + \frac{1}{Q_{\text{clamping}}} + \frac{1}{Q_{\text{intrinsic}}} + \frac{1}{Q_{\text{other}}}.$$

Hence, the overall Q-factor is limited by the loss mechanism contributing to the damping the most. Therefore, it is important to quantify all individual Q-factors for each major dissipation mechanism before being able to start optimizing the overall Q-factor.

4.1.1 Gas damping

The medium, in which the resonator is placed, has a significant impact on its Q-factor. Since the oscillators used in this thesis are only placed in gaseous media, the two fundamental regimes of gas damping will be discussed in the following. These are the fluidic and the ballistic regime.
Gas damping occurs due to the interaction of the surrounding gas molecules with the surface of the mechanical resonator. The behaviour of the resonator is mostly pressure-dependent and the underlying regime can be determined by calculating the so-called Knudsen number Kn [29]

$$Kn = \frac{\lambda_f}{L_r}. \tag{4.2}$$

Here, L_r is the physical length scale of the resonator and λ_f is the mean free path of the surrounding gas, that can be approximated as

$$\lambda_f = \frac{k_B T}{\sqrt{2}\pi d_{\text{gas}}^2} \frac{1}{p},$$

with the Boltzmann constant k_B, the temperature T, the average diameter of the gas molecules d_{gas} and the gas pressure p [29].
The gas damping regime is fluidic for $Kn < 1$. Here, the gas can be approximated as a continuous fluid due to the dimension of the resonator being large compared to the mean free path length of the gas. For the opposite case, $Kn > 1$, the regime is ballistic. This corresponds to a low vacuum for micrometer-scale structures. The damping of the oscillator occurs due to the impact of individual gas molecules [29]. The difference between the two regimes is schematically illustrated in Fig. 4.1. As the damping effects are generally stronger in the fluidic regime, these losses can be reduced by reducing the pressure of the surrounding medium.
The two most common gas damping mechanisms affecting micromechanical resonators are squeeze-film (SF) and drag force (DF) damping. Squeeze-film damping occurs when gas that is confined between two surfaces is moved by the oscillating resonator, leading to energy dissipation. This is the case for the structures in this thesis, as the oscillating membranes are close to the substrate they

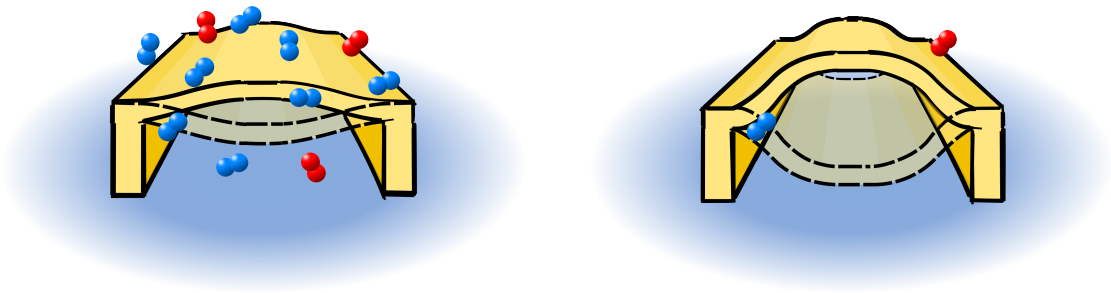

(a) (b)

Figure 4.1: Schematic of micromechanical resonators, fabricated in this thesis, in **(a)** ambient and **(b)** vacuum conditions. The oscillation amplitude is significantly decreased in the fluidic regime, under ambient pressure, due to increased collision rate of the membrane with air molecules. In the ballistic regime, under vacuum pressure, the mean free path of the gas molecules is increased, meaning there is less damping due to the lower collision rate with the oscillator.

are attached to. Drag force damping describes the general resistance against the oscillations of the resonator caused by surrounding gas molecules [31].
The resulting Q-factors for the two mechanisms were analytically approximated for a long beam resonator in the fluidic regime by Bao [32] as

$$Q_{\mathrm{SF-fluidic}} = \frac{\rho h d_0^3 \omega}{\mu B^2}, \tag{4.3}$$

$$Q_{\mathrm{DF-fluidic}} = \frac{\rho B h \omega}{8\mu}. \tag{4.4}$$

Here, ρ is the mass density, B the width and h the thickness of the beam, ω is the frequency of the beam's vibrational mode and d_0 is its distance to the substrate. The kinematic viscosity of the gas is given by μ.
For the ballistic regime, the Q-factors, as derived by Bao [33], are given by

$$Q_{\mathrm{SF-ballistic}} = (2\pi)^{\frac{3}{2}} \rho h \omega \left(\frac{d_0}{L}\right) \sqrt{\frac{RT}{M_m}} \frac{1}{p}, \tag{4.5}$$

$$Q_{\mathrm{DF-ballistic}} = \frac{\rho h \omega}{4} \sqrt{\frac{\pi}{2}} \sqrt{\frac{RT}{M_m}} \frac{1}{p}, \tag{4.6}$$

where L is the characteristic length scale of the resonator, R is the universal gas constant, T is the gas temperature, p is its pressure and M_m is the molar mass of the gas.

4.1.2 Clamping radiation losses

Another significant damping source is clamping radiation loss. This occurs when vibrational energy of a mechanical resonator propagates into its support structure, as illustrated in the schematic Fig. 4.2. These losses depend heavily on the geometry of both the resonator and its anchoring points [34].

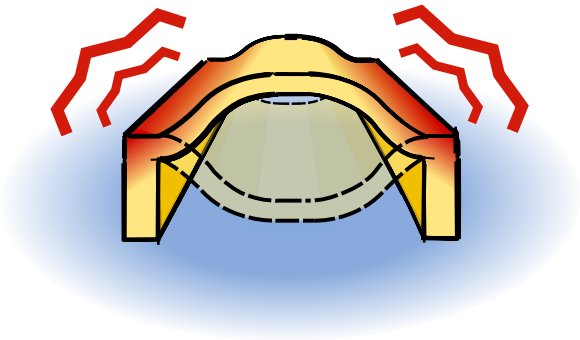

Figure 4.2: Schematic of clamping radiation losses in micromechanical resonators used in this thesis. Part of the vibrational energy from the membrane is lost due to dissipation into the anchoring points of the support structure.

Here, losses in clamped beams anchored to relatively thick support structures of the same material are discussed.
The Q-factor for clamping radiation losses was analytically calculated for cantilevers (beams clamped at one end) in [34] as

$$Q_{\mathrm{cl}}^{-1} = A\frac{B}{L}\left(\frac{h}{L}\right)^4 , \tag{4.7}$$

where the numerical coefficient A is a function of the Poisson's ratio ν. For the resonator material used in this thesis (IP-S resist) the Poisson's ratio is $\nu = 0.3$ [35], which results in a coefficient of $A = 0.31$ [34].
Since the structures in this thesis are typically doubly clamped, the coefficient A has to be adjusted for this case. For doubly clamped beams, A is a factor of 145.1 larger than for cantilevers [34], leading to $A = 45$ for the material IP-S.
Several methods of suppressing radiation losses have been developed. One approach is increasing the impedance mismatch between the resonator and substrate by alteration selection of the substrate material and thickness [36]. Other methods include inducing acoustic bandgaps via implementing phononic crystals, effectively shielding membrane modes from their support structures [37].

4.1.3 Intrinsic losses

Next, intrinsic losses are discussed. They are loss mechanisms that occur both inside and on the surface of the oscillator. Intrinsic losses can be divided into friction losses and fundamental losses.
Friction losses stem from the irreversible motion of atoms during vibration of the material. This is best described by anelasticity models such as the Zener model, which is done in the following, based on the derivation in [29]. Anelastic materials show both elastic and viscous behavior while fully returning to their initial state when their load is removed. In such a model, strain and stress follow different time scales. The strain $\varepsilon(t)$ lags behind the induced stress $\sigma(t)$ with phase δ:

$$\begin{aligned} \varepsilon(\omega) &= \varepsilon_0 \sin(\omega t) , \\ \sigma(\omega) &= \sigma_0 \sin(\omega t + \delta) . \end{aligned}$$

Applying trigonometric identities, one can expand the stress to

$$\sigma = \varepsilon_0 E_{Re} \sin \omega t + \varepsilon_0 E_{Im} \cos \omega t \,, \tag{4.8}$$

where

$$E_{Re} = \frac{\sigma_0}{\varepsilon_0} \cos \delta, \quad E_{Im} = \frac{\sigma_0}{\varepsilon_0} \sin \delta$$

are the real and imaginary part of the complex Young's modulus $E_Y = E_0 + iE_{Im}$ [38]. The resulting stress consists of one component in phase with the strain and one $\pi/2$ out of phase with the strain. Explicitly calculating the stored energy W and dissipated energy per cycle ΔW, using Eq. (4.8), one gets

$$\Delta W = \pi E_{Im} \varepsilon_0^2 \,,$$
$$W = \frac{1}{2} E_{Re} \varepsilon_0^2 \,.$$

Inserting this into the general definition of the Q-factor in Eq. (4.1) results in a formulation of the intrinsic friction Q-factor, also known as loss-tangent:

$$Q_{intr} = \frac{E_{Im}}{E_{Re}} = \tan \delta^{-1} \,. \tag{4.9}$$

Intrinsic friction losses generally depend on the oscillation frequency and temperature. However, an approximation using Eq. (4.9) is made. Here, E_{Im} is the loss Young's modulus and E_{Re} is the storage Young's modulus, which are both given material properties for the used membrane material IP-S [35]. Surface losses can also be the dominating loss channel for structures with sub-micrometer thickness [39], which is negligible for the structures in this thesis, as the membrane thickness of the fabricated structures is larger with $h > 1\,\mu\text{m}$.

A notable fundamental loss channel is thermoelastic damping (TED). In this loss mechanism, bending of the oscillator induces a temperature gradient within its material, as compressed parts of the resonator heat up. This leads to energy dissipation of part of the oscillation energy into thermal energy, in form of heat flow [38]. This is schematically depicted in Fig. 4.3.

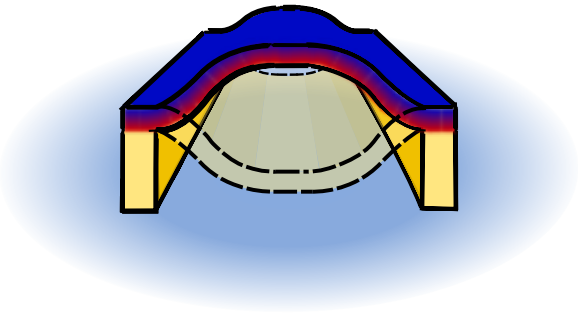

Figure 4.3: Schematic of thermoelastic losses, where the parts of the membrane that get compressed while bending heat up (red) and parts that expand cool down (blue). The resulting temperature gradient induces energy dissipation in form of heat flow.

The resulting Q-factor from TED was calculated analytically by Zener [40] as

$$Q_{TED}^{-1} = \frac{\alpha^2 T E}{\rho C_p} \frac{\omega \tau_{TED}}{1 + \left(\omega \tau_{TED}\right)^2} \tag{4.10}$$

with the thermal relaxation time τ_{TED}, given by

$$\tau_{TED} = \frac{h^2 \rho C_p}{\pi^2 \kappa} .$$

Here, α is the thermal expansion coefficient, C_p is the specific heat capacity at constant pressure and κ is the thermal conductivity of the material.
Intrinsic losses can be suppressed using the principle of dissipation dilution, which is derived in the following in Section 4.3.

4.2 Q-factor estimations for fabricated membranes

Using the analytical expressions for the Q-factors of various losses, as presented in Section 4.1, estimations of their order of magnitude were made. This is done to identify the limiting loss channels that need to be minimized.
The fabricated membranes in this thesis are made out of polymerized IP-S photoresist. Most material properties were given by the manufacturer, listed in [35]. However, for thermal coefficients, properties of a comparable polymer (PMMA) were used as a replacement, as listed in [41].
The calculation of gas damping also requires some additional parameters. For the diameter of air particles, the diameter of nitrogen (N_2) $d_g = 370\,\mathrm{pm}$, is assumed [42]. The kinematic viscosity of air for ambient pressures is assumed as $\mu = 15.1 \times 10^{-6}\,\mathrm{m^2\,s^{-1}}$ [43] and the molar mass of air as $M_\mathrm{m} = 28.96 \times 10^{-3}\,\mathrm{kg\,mol^{-1}}$[44]. The universal gas constant $R = 8.314472\,\mathrm{J\,mol^{-1}\,K^{-1}}$ is taken from [45].
Additionally, some Q-factor calculations require the resonance frequency of the oscillator. It is approximated with the formula for stressed strings [29] as

$$\omega_\mathrm{n} = \frac{n\pi}{L}\sqrt{\frac{\sigma}{\rho}}, \tag{4.11}$$

with the mode number n, oscillator length L, stress σ and the density of the material ρ. Here, $n = 1$ is assumed, as the fundamental mode is of greatest interest, and the stress is assumed to be of a value that corresponds to a length change of the oscillator of 6%, because of the typical shrinkage effects of IP-S [35]. This is calculated using the well-known relation [29]

$$\sigma = E \cdot \varepsilon \tag{4.12}$$

where E is the known Young's modulus of the material and the strain ε can be calculated with [29]

$$\varepsilon = \frac{\Delta L}{L_0}. \tag{4.13}$$

Here, ΔL is the relative length change of the oscillator due to the stress and L_0 is its original length.
Calculating the Knudsen number, using Eq. (4.2), shows that the used structures operate in the fluidic regime in ambient ($p = 1.01\,\mathrm{bar}$ as measured in the lab) and in the ballistic regime for vacuum conditions ($p = 1 \times 10^{-6}\,\mathrm{mbar}$ as measured in the vacuum chamber of the VFM). Therefore, the Q-factor was estimated for both regimes.
Furthermore, the losses were calculated for multiple lengths L, widths B and thicknesses h of the membranes. One used geometry was based on similar structures that were previously manufactured in our research group [12] with approximate dimensions $(50 \times 50)\,\mu\mathrm{m}^2$ and thickness $h = 1\,\mu\mathrm{m}$. Additionally, a string-like geometry of $(300 \times 20)\,\mu\mathrm{m}^2$, including thicker membranes ($h = 5\,\mu\mathrm{m}$), was evaluated.
The calculated estimates of the order of magnitude of the Q-factors for these configurations are summarized in Table 4.1.
The calculated gas damping losses in the fluidic regime can limit the total Q-factor, while they are negligible for the ballistic regime. This is why all measurements of the mechanical Q-factor are conducted using the VFM setup under vacuum conditions.

Table 4.1: Estimated orders of magnitude of the Q-factor for the different loss mechanisms discussed in Section 4.1. The calculations were made using parameters listed above for different geometries (membrane length L, width B and thickness h).

Loss mechanism	$(L \times B)$: $(50 \times 50)\ \mu m^2$		$(L \times B)$: $(300 \times 20)\ \mu m^2$	
	$h = 1\ \mu m$	$h = 5\ \mu m$	$h = 1\ \mu m$	$h = 5\ \mu m$
Fluidic SF (4.3)	10^4	10^3	10^3	10^4
Fluidic DF (4.4)	10^4	10^4	10^2	10^3
Ballistic SF (4.5)	10^{10}	10^{11}	10^9	10^{10}
Ballistic DF (4.6)	10^{10}	10^{11}	10^9	10^{10}
Clamp. radiation (4.7)	10^7	10^4	10^{11}	10^9
Intr. friction (4.9)	10^1	10^1	10^1	10^1
TED (4.10)	10^1	$< 10^1$	10^2	$< 10^1$

The Q-factor for clamping radiation losses is primarily lowered for shorter and thicker structures, which is not an issue, as long membranes will be used, as will be discussed further in the next section, Section 4.3.

Thus, the intrinsic losses (intrinsic friction and thermoelastic damping) are the only strongly limiting loss channels for the Q-factor of the used membrane structures. The estimated orders of magnitude for $(50 \times 50)\ \mu m^2$ membranes roughly align with previously recorded Q-factors of about $Q \approx 20$ for similar structures in our research group [12].

Hence, these intrinsic losses need to be suppressed, which will be done using the principle of dissipation dilution. This is discussed in the following in Section 4.3.

4.3 Dissipation dilution

As calculated in Section 4.2, intrinsic losses are the primary dissipation channel affecting the fabricated oscillators of this thesis, making it necessary to improve the intrinsic Q-factor. This is where the principle of dissipation dilution becomes relevant, which is briefly derived here, based on [29].
In principle, dissipation dilution refers to reducing intrinsic energy dissipation by applying a quasi-lossless external potential to the system. Since intrinsic material losses stem from elongation and bending of an oscillator, one can express the mechanical Q-factor of a string or membrane using the general definition of the Q-factor Eq. (4.1) as

$$Q = 2\pi \frac{W_{\text{elongation}} + W_{\text{bending}}}{\Delta W_{\text{elongation}} + \Delta W_{\text{bending}}},$$

where W is the energy stored and ΔW is the energy lost due to elongation and bending. Consequently, one can increase the Q-factor by introducing another potential, that suffers from less losses than elongation and bending. This can be done in the form of tensile energy W_{tensile}, which acts as a quasi-lossless potential, as the work done by tension is close to zero for flexural modes [46].
Using this approximation, the Q-factor for a stressed resonator can be expressed as

$$Q_{\text{dd}} = Q_{\text{int}} \cdot \left(1 + \frac{W_{\text{tensile}}}{W_{\text{elongation}} + W_{\text{bending}}}\right) = Q_{\text{int}} \cdot \alpha_{\text{dd}} \tag{4.14}$$

with the dissipation dilution factor α_{dd}.
The dissipation dilution factor can be explicitly calculated for transversal modes of a string using the mode shape

$$U_n(x,t) = \phi_n(x) u_n(t)$$

with the normalized mode shape given by

$$\phi_n(x) = \underbrace{\sin\left(\beta_\sigma x\right)}_{\text{sine shape}} + \underbrace{\frac{\beta_\sigma}{\beta_E}\left[e^{-\beta_E x} - \cos\left(\beta_\sigma x\right)\right]}_{\text{edge shape}}. \tag{4.15}$$

Here, n is the mode number, $\beta_\sigma = \frac{n\pi}{L}$ is the wave number related to the tensile stress σ and $\beta_E = \sqrt{\frac{\sigma A}{E I_y}}$ considers the flexural rigidity of the membrane. A is the cross-section area and I_y is the area moment of intertia around the y-axis of the oscillator.
The tensile, bending and elongation energy of the string can then be calculated with

$$\begin{aligned} W_{\text{bending}} &= \frac{1}{2} E I_y \int_0^L \left(\frac{\partial^2 U_n}{\partial x^2}\right)^2 \mathrm{d}x \\ W_{\text{elongation}} &= \frac{1}{8} E A \int_0^L \left(\frac{\partial U_n}{\partial x}\right)^4 \mathrm{d}x \\ W_{\text{tension}} &= \frac{1}{2} \sigma A \int_0^L \left(\frac{\partial U_n}{\partial x}\right)^2 \mathrm{d}x\,. \end{aligned}$$

The derivations of the mode shapes in the integrals are plotted in Fig. 4.4, each depending on position x relative to the total length of the oscillator L, starting from the edge of the oscillator. Both the simple assumption of a sinusoidal mode shape and the adjusted mode shape from Eq. (4.15) are depicted. The elongation in Fig. 4.4 (b) and tensile energy density in Fig. 4.4 (c) are similar for both of these cases. Hence, the exponential edge term can be neglected for the calculation of the integrals above. For the bending energy in Fig. 4.4 (a), however, this is not the case, as the energy density is highest near the clamping points.
Using the results of the integrals and Eq. (4.14), the dissipation dilution factor for a uniform rectangular beam can be expressed as

$$\alpha_{dd,1\mathrm{D}} = \frac{1}{2\lambda + \pi^2 n^2 \lambda^2} \tag{4.16}$$

with the mode number n. The parameter λ is defined as

$$\lambda^2 = \frac{1}{12\varepsilon_{\mathrm{avg}}} \frac{h^2}{l^2}$$

with the volume-averaged tensile strain ϵ_{avg}, beam thickness h and beam length l [47]. Here, the term proportional to λ encompasses contributions near the clamped edges and the term proportional to λ^2 accounts for the anti-nodes along the beam. An additional non-linear term becomes significant for large oscillation amplitudes [29], which is negligible for the fabricated structures in this thesis.
Looking at Eq. (4.16), the dissipation dilution factor, which needs to be increased to achieve a higher Q-factor, primarily depends on the geometry of the oscillator and the tensile strain. In particular the thickness h needs to be small and the length l and strain ε need to be large for a higher dissipation dilution factor. This is illustrated in Fig. 4.5, where a constant tensile stress corresponding to a relative length change of 6 % is assumed. The smaller and thinner the membrane is, the larger the dissipation dilution factor becomes, which is additionally visualized through 3D models of the membranes.
The geometry and the increase of tensile strain need to be created by adjusting fabrication parameters, which is discussed in the following in Chapter 5 .

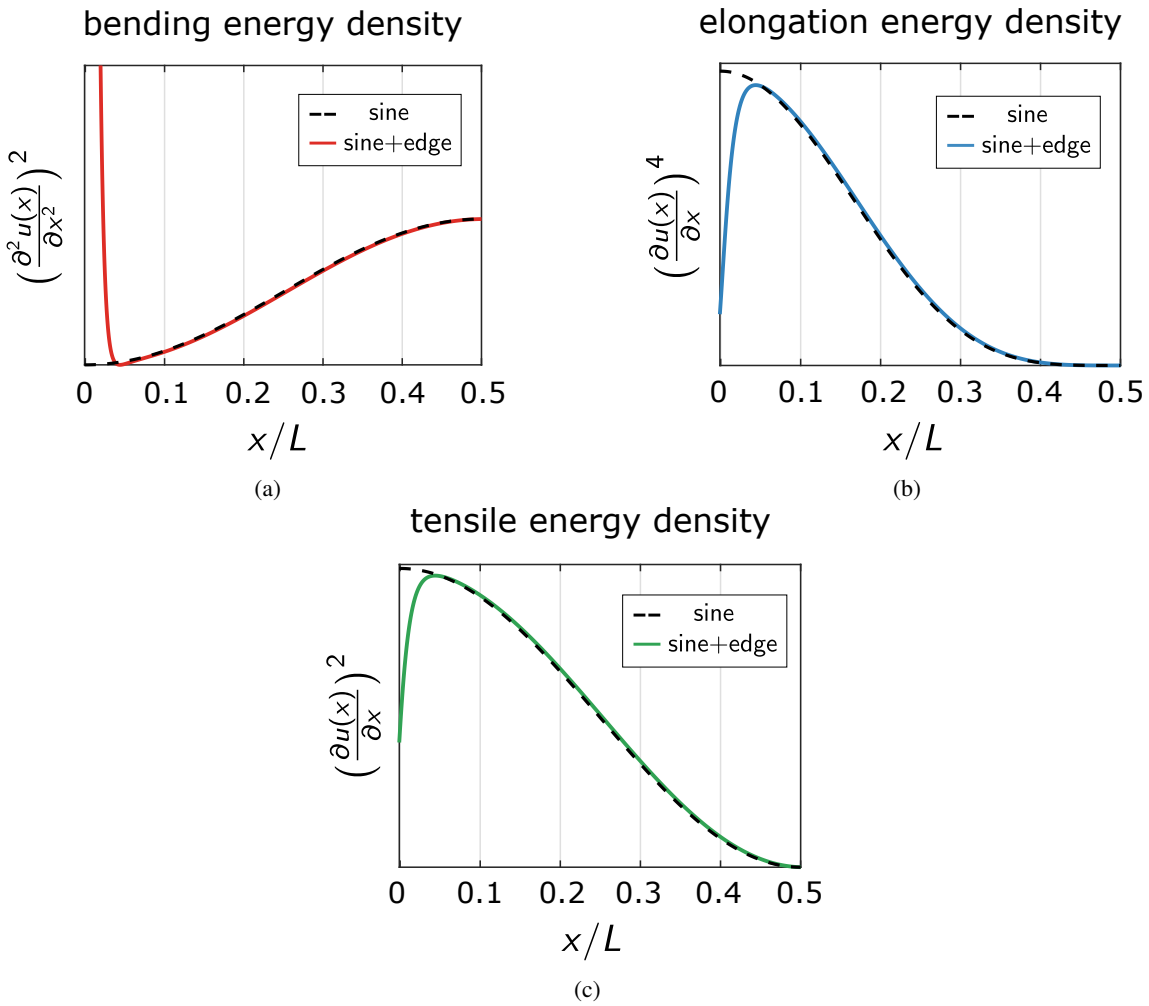

Figure 4.4: Plots of different energy densities for the oscillator, with and without the exponential correction term Eq. (4.15). The energy densities are plotted as functions of position x relative to the total oscillator length L, starting from a clamping point. The edge term is negligible when calculating the integral for **(b)** elongation and **(c)** tension, while there is **(a)** a strong contribution at the edges for bending.

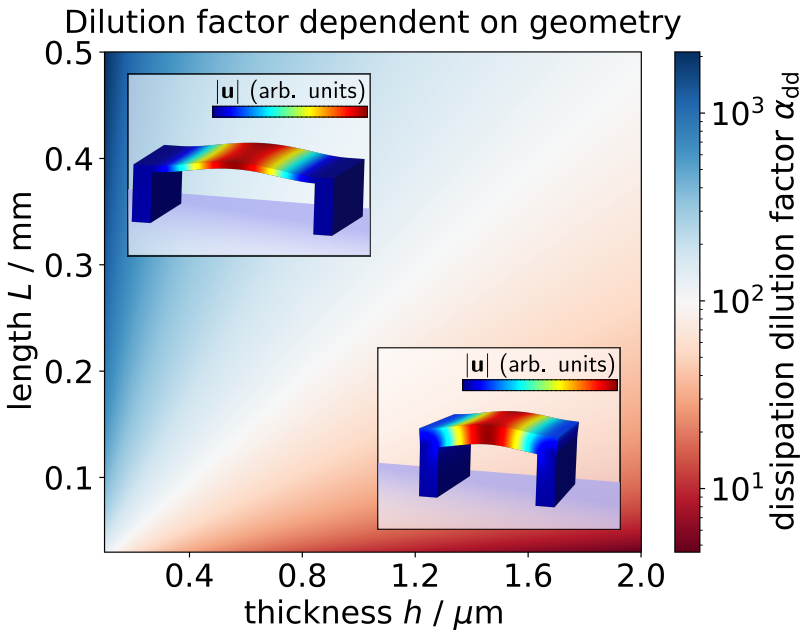

Figure 4.5: Plotted dissipation dilution factor (4.16) as a function of thickness h and length L of an oscillator. A constant tensile stress corresponding to a shrinkage/expansion of 6 % is assumed. The longer and thinner the oscillator, the higher is the dissipation dilution factor. This is additionally visualized by 3D models (not to scale).

CHAPTER 5

Fabrication with the Nanoscribe system

The core part of this thesis lies in the fabrication of the membranes used for the optomechanical systems of our research group. This is done by 3D direct laser writing, where liquid resin is locally polymerized by a focused laser beam. This way, it is possible to write structures with details in the sub-micrometer scale. The machine used is the commercial Nanoscribe PPGT+ system [1]. The general working principle of 3D direct laser writing and relevant writing parameters and properties of the Nanoscribe are presented in Section 5.1. In particular the adjustments needed to achieve higher Q-factors, as discussed in the previous Chapter 4, are further detailed.
In Section 5.2, first printed membranes and their examination process are demonstrated. This includes the introduction of dose-tests. Printing an array of membranes, where multiple parameters are varied, is an efficient way of systematically optimizing the structures. This principle is applied for all of the fabrication of this thesis.

5.1 Working principles of the Nanoscribe

The fabrication of all mechanical oscillators (membranes) for this thesis is made with a commercial 3D direct laser writing system (Nanoscribe PPGT+), which belongs to the group of Stefan Linden. The general working principle of 3D direct laser writing and the functionality of the Nanoscribe are introduced below.

5.1.1 3D direct laser writing

The Nanoscribe makes use of 3D direct laser writing to create structures with features on a sub-micrometer scale out of liquid resin. A laser is employed to cause polymerization of the resin, which hardens it. The underlying process is free radical polymerization, which involves the forming of polymer chains caused by the energy of the laser light [48].
To only polymerize a small area of the resin, the Nanoscribe makes use of two-photon-absorption (2PA) [49]. Since 2PA is a strongly non-linear process with respect to the required laser power for proper polymerization of the resin, an ultra-short fs-pulsed laser with peak powers of 25 kW is employed [50]. With these laser parameters, two IR-photons are needed to reach the polymerization threshold of the resin. This only takes place around a spheroidal volume around the focal spot of the laser beam, where

[1] Nanoscribe GmbH & Co. KG: https://www.nanoscribe.com/

the light intensity is sufficient. Depending on the used objective, the polymerized volume, a so-called "voxel", has a lateral resolution of down to sub-micrometer size [51].
In contrast, if a UV-laser would be employed instead, where one-photon absorption (1PA) is the dominant polymerization process, the polymerization threshold would be reached within the entire laser light cone [52]. This would prevent precise spacial control of the polymerization procedure, which is required for printing in a 3-dimensional space. The comparison between 1PA and 2PA is visualized in Fig. 5.1.
To explain the working principle of the printing process with the Nanoscribe PPGT+, a closer look at the optical cabinet of the system is illustrated in Fig. 5.2. For writing structures, a droplet of liquid resin is directly applied onto a substrate, which will hold the printed structures. In the case of this thesis, the used substrates are half-inch mirror substrates with transmissions of $(10 - 100)$ ppm, onto which membranes are directly printed on. This way, the mechanical oscillators are directly integrated into the cavity, when using these mirrors in the VFM setup, as discussed in Section 3.1. The chosen material for the membranes is the IP-S resin by Nanoscribe [35], because of the superior optical quality and minimal surface roughness of IP-S resin prints, compared to other commercial Nanoscribe resins [15].
In the optical cabinet of the Nanoscribe, the substrates are placed into a substrate holder, that is attached to a piezo stage. The objective with the in-coupled laser beam is then dipped into the liquid resin, that was applied on the substrate. This reduces the amount of optical interfaces between the objective and the photo resin, reducing the overall optical aberrations during the printing procedure [54]. There

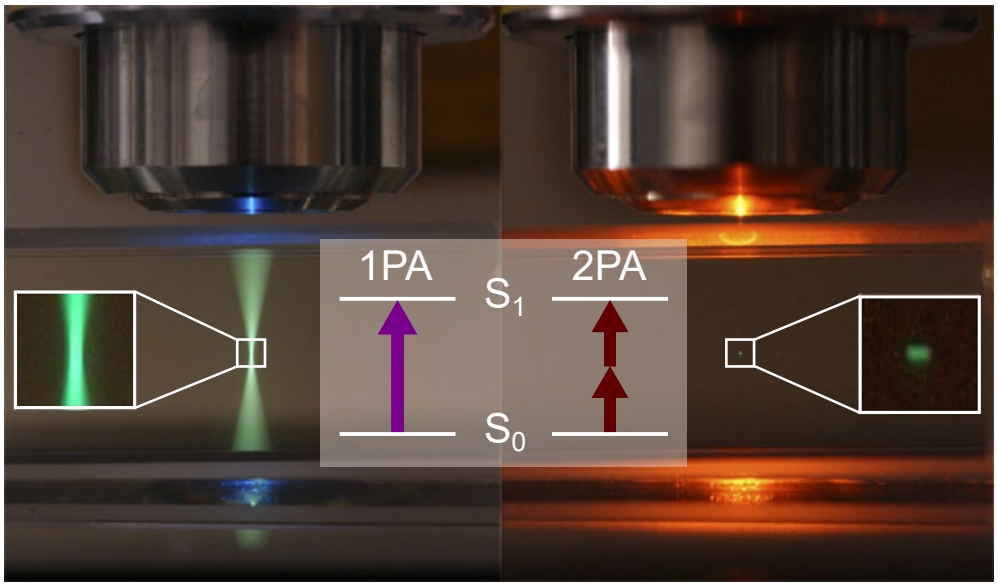

Figure 5.1: Comparison of the intensity distributions of 1PA and 2PA processes via fluorescence imaging. For 1PA processes, a single photon is sufficient to provoke the polymerization process by exciting state S_1 of the resin, which is visualized by the level scheme. Consequently, the intensity threshold is reached within the entire laser light cone. For 2PA processes, two-photons are needed to reach the excited state of the resin, also illustrated in the level scheme. Here, the intensity distribution of the light is confined around the focal spot of the laser. Therefore, only a small volume of a photo-resist is polymerized. Image taken and modified from Steve Ruzin and Holly Aaron, UC Berkeley [53].

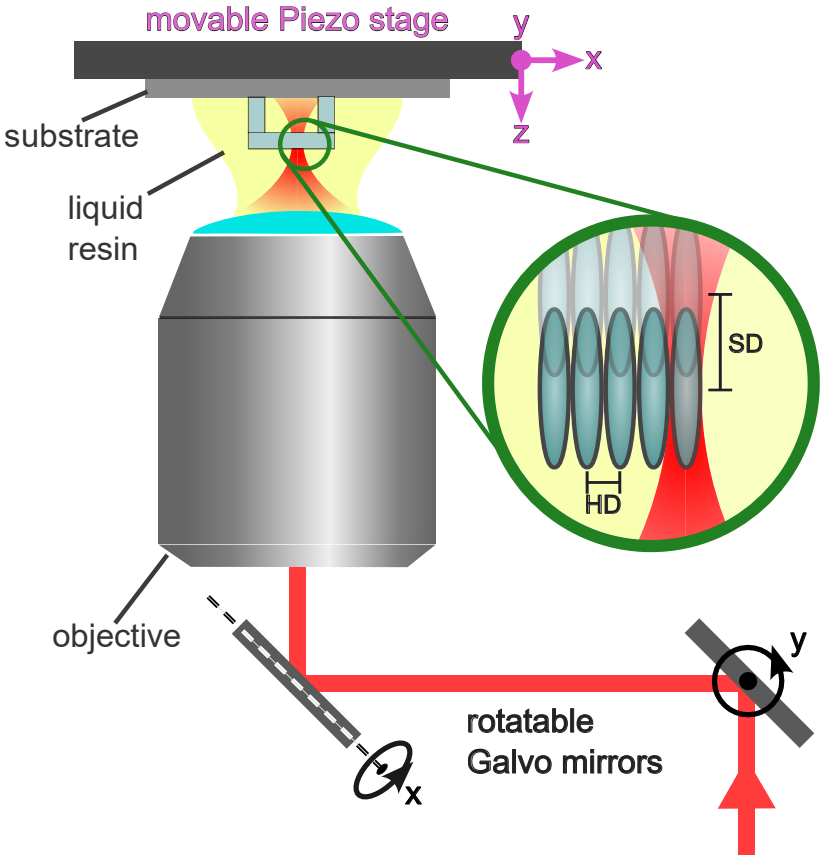

Figure 5.2: Schematic of the inside of the optical cabinet of the Nanoscribe PPGT+. The substrate, on which the structures are printed on, is mounted onto a substrate holder, which is movable in all spatial directions by a piezo stage. During the writing process, the exchangeable objective is dipped inside the photo-resin, which is applied on the substrate. The laser light needed for polymerization of the resin is coupled into the objective. The beam's trajectory and therefore its focus position can be adjusted via rotatable so-called galvo mirrors. Therefore, one can either move the substrate relative to the beam focus (piezo mode) or the beam focus relative to the substrate (galvo mode). With these writing modes, one can write structures such as the illustrated membrane. As shown in the zoomed-in segment, the written structures consist of individually polymerized voxels with respective distances to one another in x-direction, set by the hatching distance (HD), and in z-direction, set by the slicing distance (SD).

are several available objectives with different use-cases. The 63x-objective, which is mostly used in this thesis, features the minimum voxel dimensions possible (lateral resolution $a_{xy} = 340\,\text{nm}$, axial resolution $a_z = 826\,\text{nm}$ [51]), as it is designed for the smallest feature sizes.
These voxels of the resin are polymerized around the laser's focal spot. Here, the trajectory of the incoming laser beam is adjustable via two rotatable "galvo mirrors", making it possible to move the laser beam focus relative to the substrate in the x-y plane. Structures are written this way when using the "galvo mode" of the system. Here, the distance along the z-axis is adjusted via the piezo stage, that the substrate holder is attached to. Alternatively, the substrate can also be moved in the x-y plane relative to the beam focus via the piezo stage, when using the "piezo mode". Using either of the writing modes, structures such as the depicted membrane can be written out of multiple voxels. The

distance of the voxels from one another in x-direction can be set via the hatching distance (HD) and in z-direction via the slicing distance (SD), as also shown in Fig. 5.2.

5.1.2 Relevant properties and writing parameters

As derived in Section 4.3, the intrinsic Q-factor, which is the limiting factor for membranes fabricated out of IP-S, can be improved by manufacturing long and thin membranes that are under tensile strain. Using the writing modes explained above, the geometry of written structures can be directly adjusted. This is done either manually in the programming application DeScribe for designing Nanoscribe prints or by creating a CAD model first (i.e. with Inventor) and importing it into DeScribe. Several writing parameters can be changed with either option. Although, creating structures manually offers more flexibility while using CAD models makes the creation of different geometries easier. It has to be noted that the exact geometry, as specified in the program, is never fully realized. This is especially the case for the thickness of membrane layers, that is limited by the axial resolution of the voxels.
Creating tensile stress on the membrane is less straight forward. However, one can make use of one of the side-effects of two-photon polymerization. During the printing process and development, the resin and therefore the written structures undergo shrinkage [55]. This effect is usually undesired and can be suppressed by adjusting the development process. After writing a structure onto a substrate, one needs to remove the excessive un-polymerized resin. This is done by using the developer propylene glycol methyl ether acetate (PGMEA), that is later removed by rinsing with isopropyl alcohol (IPA). It has been demonstrated that subsequent UV-treatment of the printed structures before drying them can reduce the shrinkage significantly [56]. This benefits the structural integrity of the designs and has been done previously in our research group to achieve higher optical quality of the membranes. For this thesis, this is not the case, as the effect of shrinkage is used to create tensile strain in the membranes. As the supporting structures of the membrane are written first and serve as anchoring points for the membrane layers, a shrinkage of the membrane can lead to tensile stress, as illustrated schematically in Fig. 5.3. The amount of shrinkage is highly material-dependent and for IP-S the volume gets reduced by $(2-12)\,\%$ [35]. Several writing parameters can be varied to try to maximize the strain on membranes.
Apart from the hatching and slicing distance, one can also set the "scan speed" $ScSp$ (writing speed) and relative "laser power" $LP = (0-100)\,\%$. The reachable scan speeds vary largely for the different writing modes. The piezo mode makes use of relatively slow scan speeds of up to the order of $ScSp = 1\,\mathrm{mm\,s^{-1}}$. The galvo mode on the other hand can use fast scan speeds of up to the order of $ScSp = 100\,\mathrm{mm\,s^{-1}}$, depending on the resolution of the used objective. However, the increased writing speed of the galvo mode comes at the cost of less consistent voxel shapes due to increased optical aberrations near the ends of the maximum printing field [57]. This can affect the optical quality and stability of the created structures.
The maximum printing field also depends on the used objective for both writing modes. When trying to write structures larger than about $300\,\mu\mathrm{m}$ with the 63x-objective, the print has to be split up into multiple blocks, which is not desirable as it would split up parts of the membranes. Another notable difference between the piezo and galvo writing mode is the lack of tilt-correction for the latter. As the half-inch mirror substrates are enclosed within a full-inch aluminum ring adapter, there often is a slight tilt angle of the substrate surface relative to the incoming laser beam. In the piezo mode, this tilt can be compensated for automatically by using the galvo mirrors. As tilt correction is not possible in the galvo mode, one has to make sure that the written structures are properly attached to the mirror by

adjusting the structure's design.

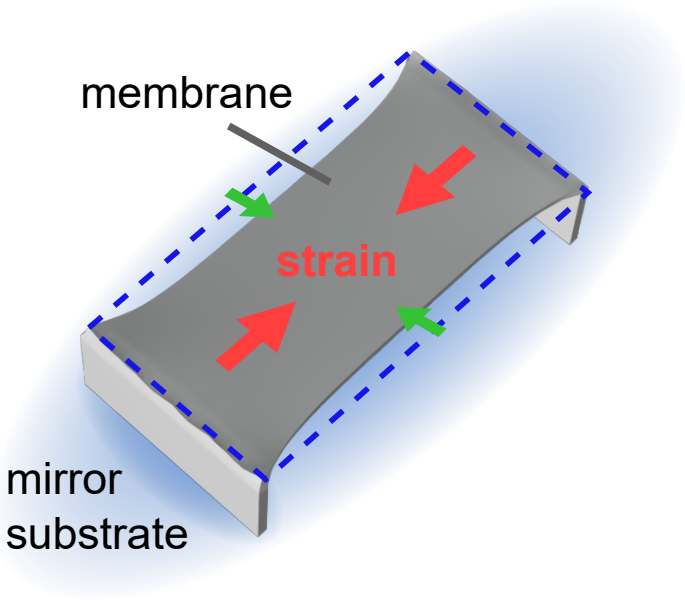

Figure 5.3: Schematic of using the intrinsic shrinkage of the resin to create strain in the membrane. The membrane is anchored to support feet-like structures, which are written before the membrane layers. Subsequent shrinkage of the membrane layers leads to strain, as the membrane can not contract freely.

5.2 Starting point for membrane fabrication

In this section, early prints and their evaluation are discussed, as this gives a good overview of the overall working procedure, that is applied throughout this thesis. The initial approach of fabricating higher mechanical Q-factor membranes was applying known parameters for achieving good optical quality, as used previously in our research group [15]. These were then adjusted iteratively, to optimize the mechanical Q-factor.
This meant starting with the piezo writing mode with the 63x objective, which can achieve a low surface roughness of < 5 nm (root-mean-square surface profile variation) [12]. Additionally, UV-curing was used for higher optical quality for the first prints, as discussed above.
The initial design of the membranes is also closely inspired by the previous work in our research group [12] and was made in DeScribe, as shown in Fig. 5.4. The relatively thin membrane is written with crossed layers (woodpile structure) to increase its stability and optical quality. It is doubly supported by thicker feet structures. The base of these support structures is widened for more stability. The resulting increased contact area between the feet and the substrate also ensures that the print adheres to the substrate, which did not happen in firsts tests without the widened base. Here, the right balance between stability and size of the support structures has to be found, as the printing process in piezo mode can take several days, when printing multiple membranes.
With this design, valid parameter ranges that produce stable prints need to be experimentally determined. This is done with a dose test. Here, an array of structures of identical geometry is printed while both the laser power as well as the scan speed can be varied. The parameter ranges that produce stable results vary widely depending on the geometry of the written structures. Although previously used parameters were taken as a reference, the optimal parameters change over time as they depend on factors such as the resin age or the cleanliness of the used objective.
A small array of membranes has been printed with a constant scan speed $ScSp = 50\,\mu\mathrm{m\,s^{-1}}$ and varying laser powers from $LP = (17 - 26)$ % in 3%-steps to sweep the laser dose, which is illustrated in Fig. 5.5. Each of the membranes has a distance to the mirror substrate of $d = 8\,\mu$m, a length of $L = 30\,\mu$m, a width of $B = 30\,\mu$m and is $t = 1\,\mu$m thick. The supporting feet structures are 5 µm thick at the top, becoming wider towards the bottom up to 13 µm and are printed at a higher scan speed to reduce the printing time. This can be done, as higher scan speeds primarily decrease the optical quality, which is only relevant for the membranes. As each print has some variance in its structure due

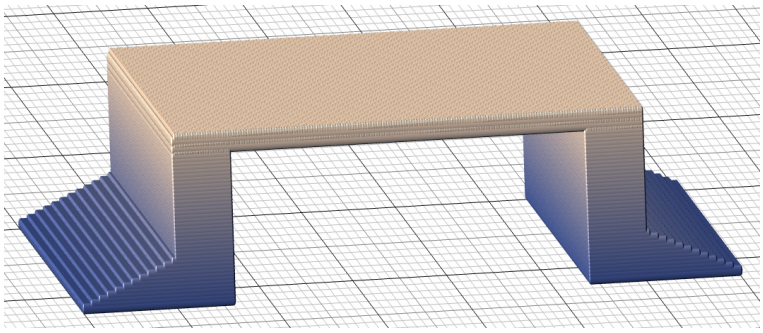

Figure 5.4: Membrane design made with DeScribe for piezo mode membrane prints. The thin membrane layers are doubly supported by pillar-like feet. The support structures have widened bases to increase the contact area between the prints and substrate. This is done to make sure that the structures adhere to the substrate.

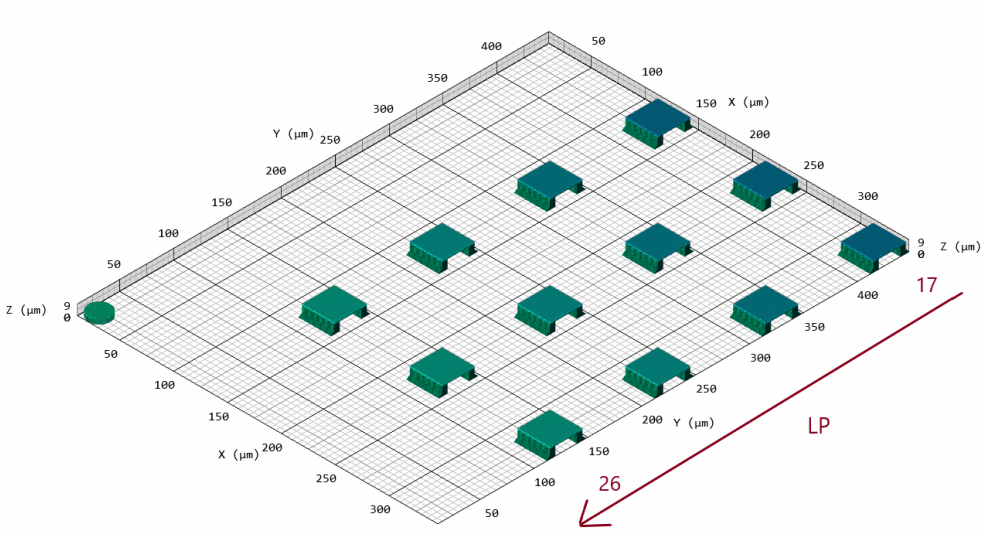

Figure 5.5: First dose test with quadratic membranes to find usable writing parameters. At a fixed scan speed of $ScSp = 50\,\mu m\,s^{-1}$ and varying laser powers from $LP = (17 - 26)$ % in 3%-steps, three membranes are printed per laser power to acquire more statistics. A cylindrical marker in the corner of the substrate serves as point of orientation for later visual inspection of the print. The chosen parameter ranges are based on previous printing jobs within the research group.

to the stochastic nature of the polymerization process, three membranes per laser power are printed. Additionally, a cylindrical marker was printed as means of orientation, when inspecting the print. The chosen hatching distance of 66 nm and slicing distance of 200 nm were also adopted from previous structures and are smaller than the recommended standard values, to achieve an even better surface roughness for optical quality.
After developing this print, it was inspected under a microscope, as shown in Fig. 5.6. This serves as a way of judging, whether a print was successful regarding its mechanical stability and surface quality. In this case, the microscope was used in dark-field configuration, where the illuminating light only scatters off the object without entering the objective, which reduces the imaging background [58]. This is a useful tool for investigating the surface details of printed membranes.
The membranes written with a laser power of $LP = 17$ % are nearly fully missing. In one case, even the support structures did not hold onto the mirror substrate. This is most likely due to the fact that the resin did not fully polymerize as the intensity threshold was not reached. For a higher laser power of $LP = 20$ %, the membranes did hold but strong artefacts are visible. For laser powers of $(23 - 26)$ % the resin seems to be close to fully polymerized. Only small artefacts at the edges of the membrane can be seen, which is more strongly pronounced for the lower laser powers. This can be identified more clearly with stronger magnification of selected membranes, shown in Fig. 5.7.
With this vague estimate of usable writing parameters, the next step is changing the design, so that dissipation dilution effects are favoured. This is done in the following, in Chapter 6.

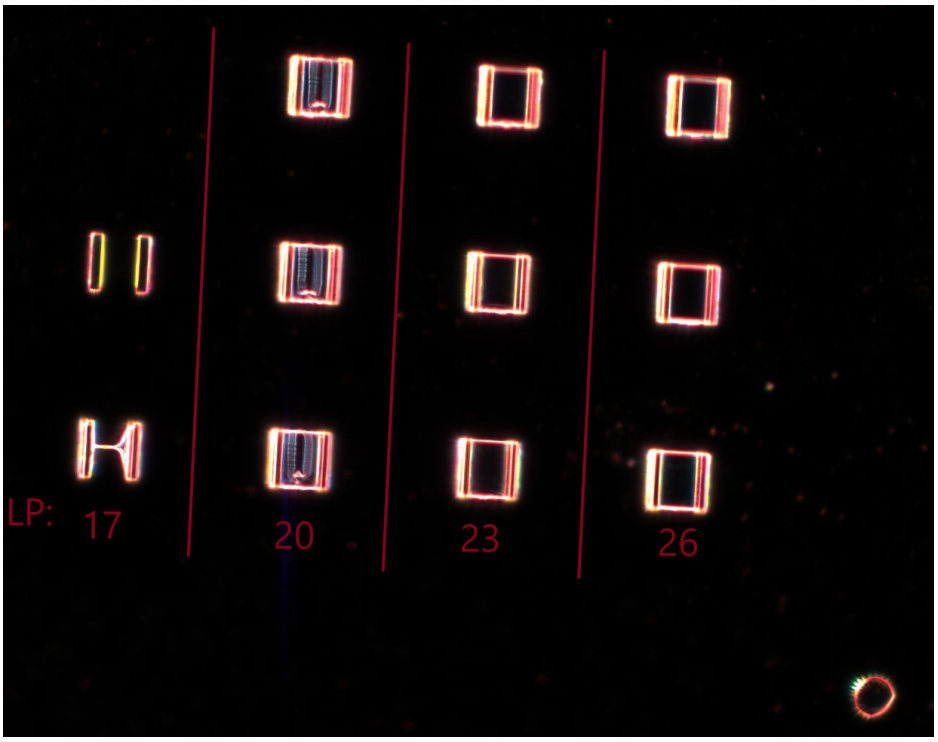

Figure 5.6: First dose test for piezo mode membranes. The image was taken with a microscope in dark-field configuration. All structures are geometrically identical in their design. Each column corresponds to a different laser power LP (in %), for which three membranes each are printed, at constant scan speed. The structures seem to be stable, starting at a laser power of about $LP = (23 - 26)$ %. For lower laser powers, the membranes are not fully polymerized, as the intensity threshold is not consistently reached.

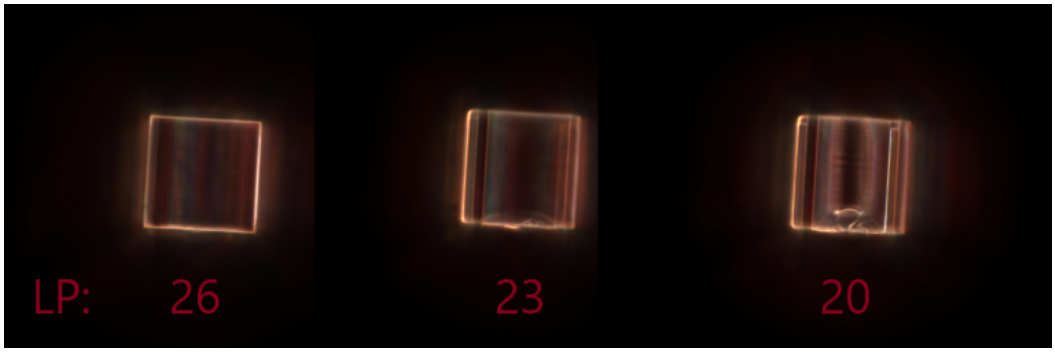

Figure 5.7: Zoom-in on selected membranes of the first dose test for piezo mode membranes. The image was taken in dark-field configuration again. Each column corresponds to a different laser power LP (in %) printed at constant scan speed. The structures seem to have a promising optical quality for the highest selected laser power. Lower laser powers lead to artefacts on the membrane surface.

CHAPTER 6

Manufacturing dissipation-diluted membranes

In this chapter, the various iterative adjustments made to the membranes, fabricated in previous works within our research group, are discussed. These adjustments aim to make use of dissipation dilution effects. For resulting mechanically stable structures with sufficient optical quality, measurements of the mechanical Q-factor were conducted with the VFM setup, as explained in Section 3.1.
In Section 6.1, length sweeps of membranes written in the piezo mode were made and measured while changing various other printing parameters.
Next, measurements of membranes printed in galvo mode are discussed. These were designed to be printed with high scan speeds, leading to more strain in the membranes. In Section 6.2, first prints made with strained membranes were measured and analyzed.
In Section 6.3, thicker membranes were printed to make use of even higher scan speeds while maintaining the stability of the structures. The resulting membranes were then treated with oxygen-plasma ashing, to decrease their thickness and achieve a higher mechanical Q-factor. To verify the effects of the treatment, the Q-factor was subsequently measured once again.

6.1 Piezo mode membranes

As derived in Section 4.3, dissipation dilution effects can come into effect for long and thin membranes that are under tensile strain. As the previously manufactured membranes were already thin with a set thickness of $h = 1\,\mu\text{m}$, the length of the membranes is increased in the following.
In preparation for this, a more elaborate dose test, based on the results of Section 5.2, was made. Here, the geometry of the membranes was adjusted to a length of $L = 100\,\mu\text{m}$ and width of $B = 25\,\mu\text{m}$. This time, higher laser powers of $LP = (35 - 60)\%$ in 5 %-steps and higher scan speeds of $ScSp = (50 - 200)\,\mu\text{m}\,\text{s}^{-1}$ in $30\,\mu\text{m}\,\text{s}^{-1}$-steps were tested. This is further detailed and shown in Appendix A.1.
To be able to see possible dissipation dilution effects, a length sweep array of piezo mode membranes was made, as depicted in Fig. 6.1. Each of the membranes has a thickness of $h = 1\,\mu\text{m}$, width of $B = 25\,\mu\text{m}$ and varying length of $L = (50 - 300)\,\mu\text{m}$. Based on the second dose test, mentioned above, the laser powers were chosen as $LP = (35 - 45)\,\%$ at a constant scan speed of $ScSp = 50\,\mu\text{m}\,\text{s}^{-1}$ for the membranes.
The membranes with a set length of $L = 300\,\mu\text{m}$ did not print properly as the maximum printing area was exceeded. Microscope images of selected membranes with a length of $L = 250\,\mu\text{m}$ are

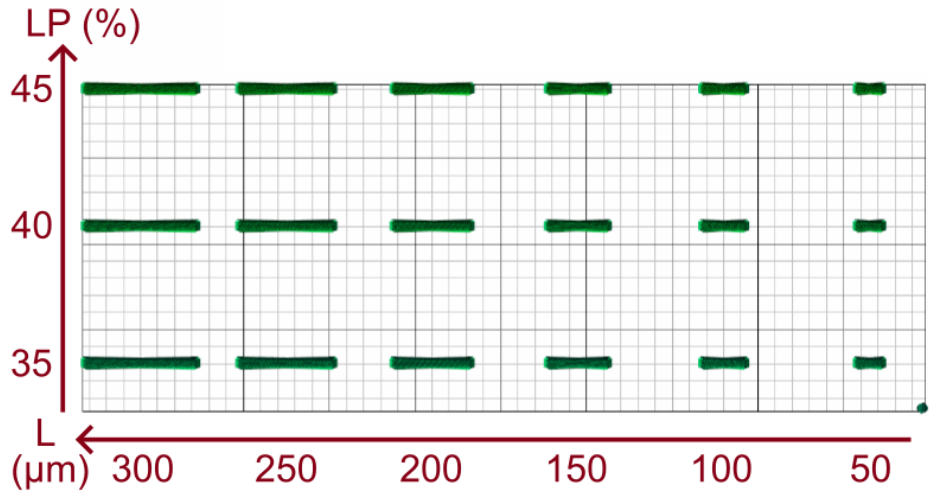

Figure 6.1: Length sweep of membranes in the piezo mode. All membranes have a thickness of $h = 1$ µm, width of $B = 25$ µm and the length is swept from $L = (50 - 300)$ µm. The laser powers are additionally swept from $LP = (35 - 45)$ % at a constant scan speed for membranes of $ScSp = 50\,\mu\mathrm{m\,s^{-1}}$.

depicted in Fig. 6.2. The membrane printed at $LP = 35$ %, as shown in Fig. 6.2 (a), completely broke down. The membrane printed at $LP = 40$ %, as shown in Fig. 6.2 (b), had loose voxel lines attached to its top layer. This was presumably caused by the first printed voxel lines not properly adhering to the membrane feet. While the membrane printed with a laser power of $LP = 45$ % at the same length looked visually stable under the microscope, building a cavity on top of the membrane was not possible, as no sufficient optical signal for locking the cavity was found. Generally, long membranes tend to be more stable for higher laser powers. Most of the shorter membranes looked visually promising for all laser powers. After the visual inspection, a measurement series of the mechanical Q-factor, which is described in Section 3.1, was attempted for all of the stable membranes under vacuum pressure of $p = 1 \times 10^{-6}$ mbar.

The relationship between the measured mechanical Q-factor and the membrane length of the stable structures, where a sufficient optical signal was found, is shown in Fig. 6.3. All measured Q-factors are around the value of $Q \approx 20$, which was already measured in previous works [12] without dissipation dilution effects and no clear correlation with the membrane length can be seen. Therefore, there is virtually no tensile strain in the membrane.

Similar prints have then been made with further adjustments, to possibly increase the strain. The usage of UV-curing in the developing process has been omitted, which increases the shrinkage of the structures after the printing process, as discussed in Section 5.1. The writing direction of the membrane layers has also been adjusted. The previously used woodpile structure for better optical quality might have affected the shrinkage negatively. It has been changed to a single writing direction for all layers, from one of the supporting structures to the other.

Both of these changes seemed to have no effect on the mechanical Q-factors, when performing measurements with a few samples at random. The anchoring of the membrane alone, as discussed in Section 5.2, does not seem to induce strain. This could be caused by the shrinkage of the resin occurring too quickly during the printing process, compared to the slower writing speed with the piezo mode. The shrinkage may already occur before the voxel lines are fully connected to both of

the support structures. Additionally, higher mechanical Q-factors of $Q \approx 1000$ have already been observed for IP-S membranes at higher scan speeds by other groups [59]. However, due to a different field of application, optical quality is neglected for these membranes.
This is why prints with higher scan speeds with the galvo mode were made next. The optimization for structures written at these high scan speeds is discussed in the following, in Section 6.2.

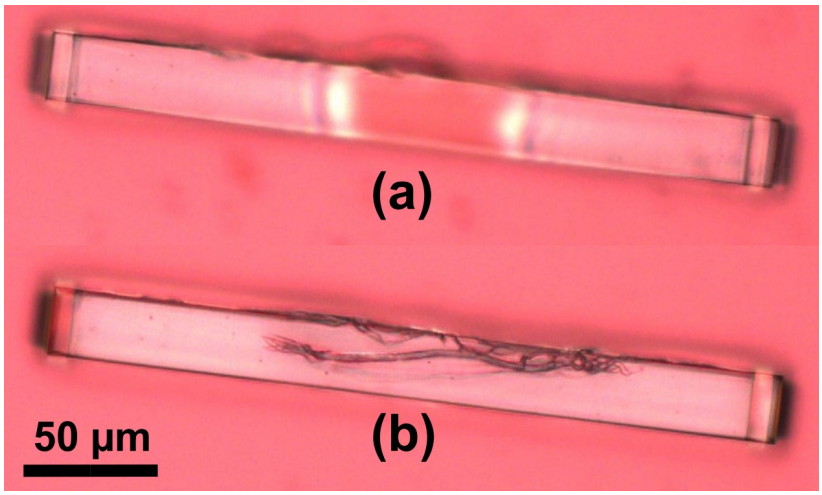

Figure 6.2: Microscope image of selected membranes of the length sweep with the piezo mode. Membranes with a length of $L = 250\,\mu m$ and a laser power of **(a)** $LP = 35\,\%$ and **(b)** $LP = 40\,\%$ are shown. The membrane printed at the lower laser power broke down completely near its center, which is why only the support structures at the side are in the image focus. The membrane printed at a laser power of $LP = 40\,\%$ is stable. However, voxel lines at one of the edges got loose and stuck to the top of the membrane.

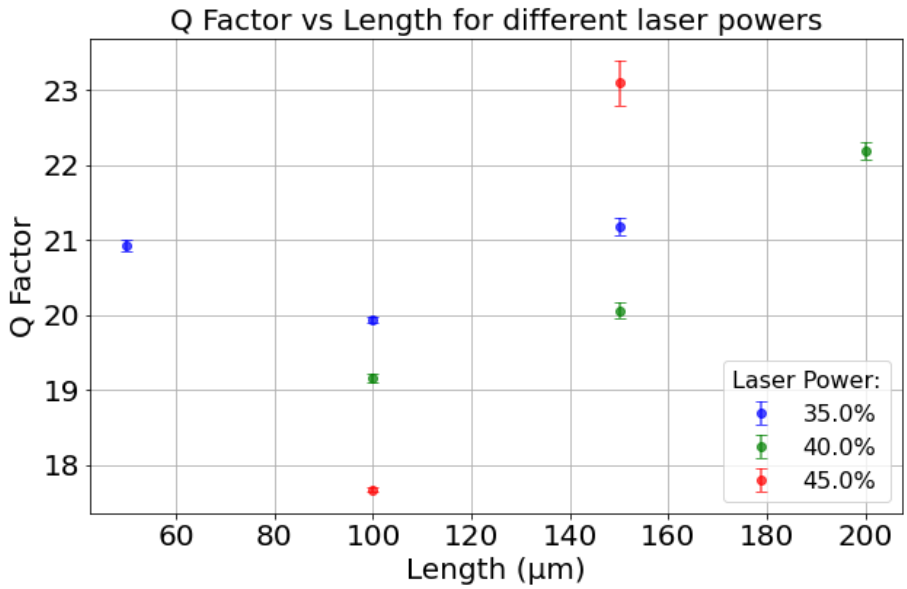

Figure 6.3: Plot illustrating the relationship of the mechanical Q-factor and the length of membranes written in piezo mode, for different laser powers at a constant scan speed of $ScSp = 50\,\mu\mathrm{m\,s}^{-1}$. A measurement was attempted for all stable membranes. In the case of no sufficient optical signal being found, no Q-factor value was registered in the plot. There is no definite correlation between the length of the membranes and their Q-factors. All Q-factors are close to the value of $Q \approx 20$, which is limited due to intrinsic losses without dissipation dilution effects occuring, as discussed in more detail in Section 4.3. The tensile strain in the membrane seems to be too low for dissipation dilution effects to occur.

6.2 Thin galvo mode membranes

In this section, prints with the faster galvo mode are presented, as the tensile strain in the membranes written at slower scan speeds was seemingly insufficient for observing dissipation dilution effects, as shown in Section 6.1. However, the steep increase in scan speed introduces further complications in fabricating stable structures. Therefore, an adjusted design of the membranes is presented first. Then, dose tests and scan sweeps with varying membrane lengths are performed to find optimal printing parameters. The Q-factor of resulting stable membranes is then measured under vacuum pressure again.

6.2.1 New print design

As there were no major issues with stability of prints with the piezo mode, the support structures were kept very slim and simple. This was also necessary to keep the printing time short. With the higher scan speeds of the galvo mode, the printing of bigger support structures is not only possible but also needed to ensure sufficient stability.
First tests in the galvo mode were made with the lower resolution 25x-objective, as this was also done in other groups to write high scan speeds structures [59]. However, this increased the surface roughness of the membranes, leading to worse optical properties. At the time, the second fiber mirror (see Section 3.2) was not installed yet, which rendered the Q-factor unmeasurable due to the optical signal being too weak. Therefore, the 63x-objective was used again for the prints in the following sections.
In galvo mode, support structures with a geometry similar to the piezo mode prints often did not adhere to the mirror substrate at all or partially detached in early testing prints, as shown in Fig. 6.4 (a). To counteract this, the bases of the support structures were iteratively broadened to increase the contact area to the substrate, as depicted in Fig. 6.4 (b). However, this still led to many instabilities and was further iterated until the final design was found.

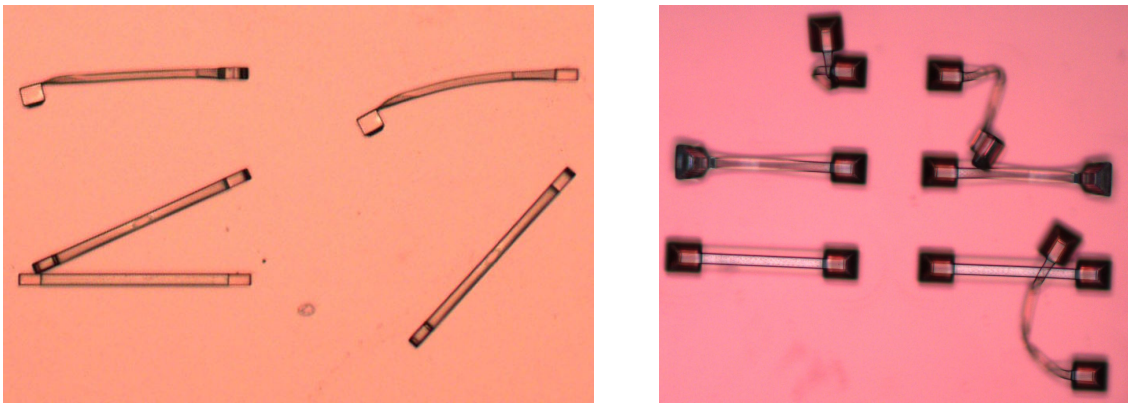

(a) (b)

Figure 6.4: Microscope images of membranes written in galvo mode with early support structure designs (with the lower resolution 25x-objective). The bases of the support structures either did not adhere to the substrate at all or partially detached, both for **(a)** bases as wide as the membranes and **(b)** a later iteration with a slightly larger base.

The final Inventor design for galvo mode membranes in this thesis can be seen in Fig. 6.5. The support structures have a pyramid shape to reduce the volume of the structure. This way the contact area to the mirror substrate is still large and the printing time is reduced. Tests have also shown that more structures were stable when the slope of the support structures does not directly blend into the membrane. That is why the junction point of the slope and the supporting pillar is below the membrane. This way, the supporting pillar and the membrane have the same width.
The length L, width B, thickness h of the membrane and other dimensions can be adjusted via variables in the corresponding Inventor file. The writing parameters, such as scan speed and laser power, are set with DeScribe after importing the CAD file of the models. To compensate for the lack of tilt correction when using the galvo mode as opposed to the piezo mode, the "interface" variable is additionally adjusted in DeScribe. The interface variable sets how deep into the substrate the writing process starts. This way, support structures still are in contact with the substrate even when the substrate is slightly tilted inside its holder. The interface variable was set to a value of 2.5 µm for most galvo mode prints, compared to the typical value of 0.2 µm for piezo mode prints.

6.2.2 Large-scale dose test for thin galvo mode structures

With the new design, a large-scale dose test was performed, to find usable writing parameters for the galvo mode with the 63x objective. Each of the membranes has a length of $L = 100\,\mu\text{m}$, which should produce stable membranes for a broad range of parameters. The other dimensions were set as described in the section above. The laser powers are varied from $LP = (40 - 100)\,\%$ in 5%-steps and scan speeds from $ScSp = (10\,000 - 100\,000)\,\mu\text{m}\,\text{s}^{-1}$ in $10\,000\,\mu\text{m}\,\text{s}^{-1}$-steps.
The array is visualized in Fig. 6.6. Here, stable membranes with a promising looking surface quality are within the green border, while flawed membranes are highlighted in red. The quality was judged by using microscope images, which are shown for selected membranes in Fig. 6.7. The depicted

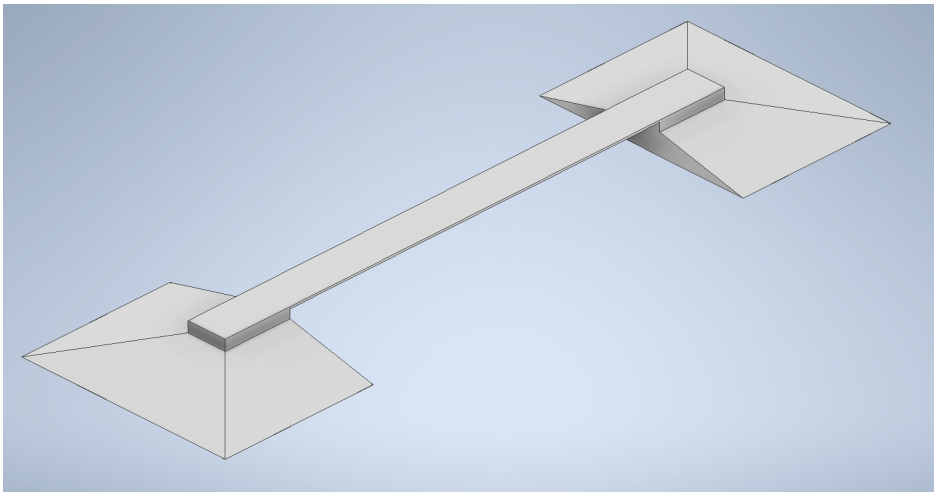

Figure 6.5: CAD model of the final design for galvo mode membranes and their support structures. The support structures are narrowed towards the top to reduce the volume and the corresponding printing time, while maintaining the increased area of the base for more contact to the substrate. The length L, width B and thickness h of the membrane, among other parameters, can be adjusted via variables in the used Inventor file. The displayed membrane design features a length of $L = 200\,\mu\text{m}$, width of $B = 20\,\mu\text{m}$ and thickness of $h = 1\,\mu\text{m}$.

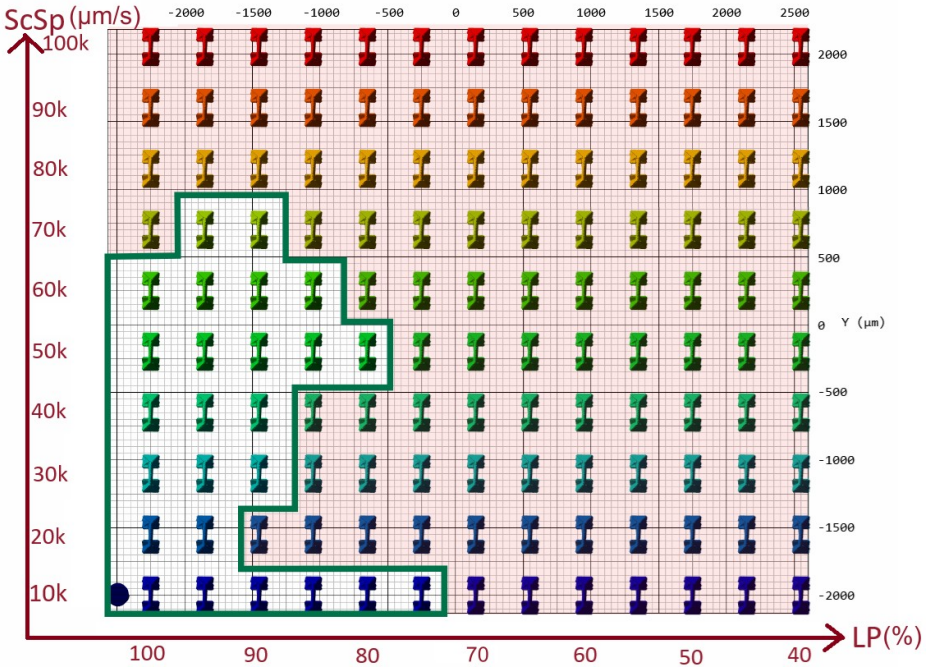

Figure 6.6: Marked DeScribe array of the large dose test for galvo mode structures written with the 63x objective. The previously shown CAD design for the membrane is imported with a length of $L = 100\,\mu\text{m}$ and used for all membranes, while laser powers are varied from $LP = (40 - 100)\%$ in 5%-steps and scan speeds from $ScSp = (10\,000 - 100\,000)\,\mu\text{m}\,\text{s}^{-1}$ in $10\,000\,\mu\text{m}\,\text{s}^{-1}$-steps along each of the axes. Visually promising membranes are within the green border, while flawed ones are highlighted in red.

membranes written at a scan speed of $ScSp = 10\,000\,\mu\text{m}\,\text{s}^{-1}$ all seem to be stable with good surface quality. For membranes written at $ScSp = 20\,000\,\mu\text{m}\,\text{s}^{-1}$, their condition gets worse the lower the laser power gets. The leftmost membrane has large artefacts or cracks near its center, the middle membrane collapsed onto the substrate and the rightmost membrane completely detached from its support structures.

Higher laser powers generally result in more stable membranes with less artefacts on the membrane surface for all scan speeds, as shown in Fig. 6.6. For laser powers of $LP \leq 70\%$ barely any membranes were fully polymerized, likely due to the laser dose being too low. For these prints, the support structures are mostly displaced. However, this was not a factor for higher doses. Another limiting factor seems to be the scan speed, where for $ScSp \geq 80\,000\,\mu\text{m}\,\text{s}^{-1}$ even the high power membranes are not properly polymerized. This might be due to the low accuracy of the printed voxel lines in galvo mode due to optical aberrations, as discussed in Section 5.1. This, combined with the high writing speed, might lead to detachments of membrane parts while printing.

The membranes generally look more promising for higher laser powers. Higher laser powers can also be beneficial for creating larger strain for fast scan speeds, as was demonstrated in [60]. Hence, the parameters used in following prints are both the maximum laser power and the maximum scan speed possible.

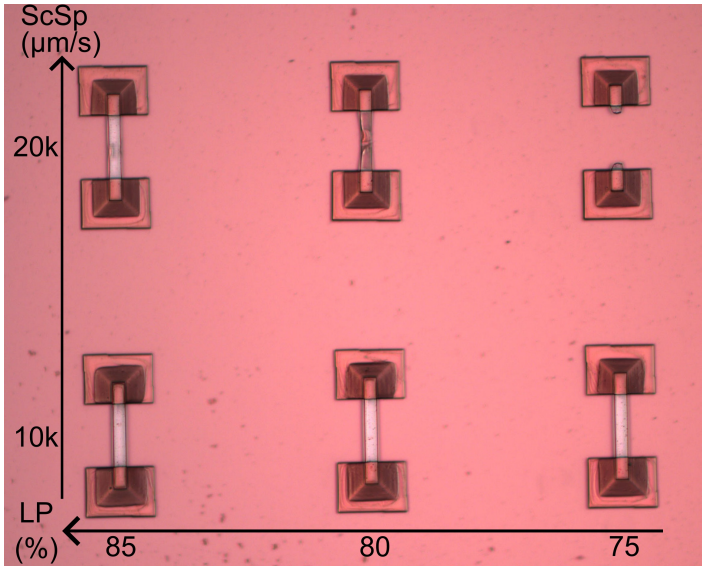

Figure 6.7: Microscope image of selected membranes from the large dose test array for galvo mode structures written with the 63x objective. While the bottom membranes, written at a scan speed of $ScSp = 10\,000\,\mu m\,s^{-1}$, look visually promising, all of the shown membranes written at $ScSp = 20\,000\,\mu m\,s^{-1}$, at the top, are damaged or broken.

6.2.3 Q-measurements of long and thin galvo mode membranes at different scan speeds

To quantify the relation between scan speed and tensile strain in the membranes, and consequently the Q-factor, a series of length sweeps is made. For scan speeds of $ScSp = (10\,000 - 60\,000)\,\mu m\,s^{-1}$, the same length sweep array is printed. Then, the mechanical Q-factor is measured for resulting stable membranes with sufficient optical quality. The array includes membranes of the lengths of $L = (50 - 250)\,\mu m$ in 50 µm-steps at high laser powers of $LP = (90 - 100)\,\%$, where each membrane is printed four times to get more statistics.
While the membranes with lengths of the previously tested 100 µm mostly printed properly, there were increasing issues for longer membranes. Increasing the scan speed reduces the maximum length of membranes, that can be printed without significant flaws. The only series of consistently stable thin ($h = 1\,\mu m$) membranes, that seem to be of decent optical quality, is for the lowest of the scan speeds $ScSp = 10\,000\,\mu m\,s^{-1}$. The corresponding microscope image is shown in Fig. 6.8.
As the Q-factor of most of these membranes was measured successfully in vacuum, it is by far the largest data set for thin galvo mode membranes. As multiple membranes for different lengths were printed properly, one can analyze the dependencies of both the Q-factor and the resonance frequency on the membrane length. The Q-factors are shown in Fig. 6.9 (a) and the frequencies in Fig. 6.9 (b). In contrast to the structures fabricated in piezo mode, a clear correlation between the length and the Q-factor can be seen. This strongly indicates the presence of dissipation dilution. Therefore, the straining of the membranes by increasing the writing speed seems to be working. However, when trying to fit the data using the derived formula for the dissipation dilution factor Eq. (4.16), the data does not seem to fit the function well. A major reason, why that is the case, is that the formula used is an approximation for strings.

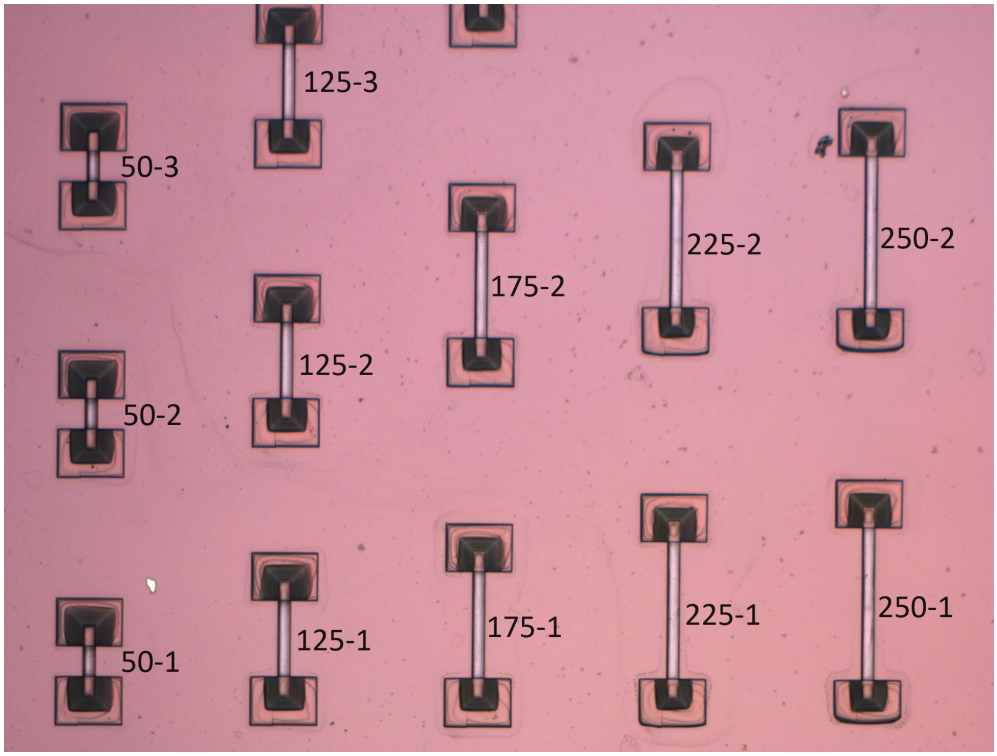

Figure 6.8: Microscope image of selected membranes written at a scan speed of $ScSp = 10\,000\,\mu m\,s^{-1}$. Each membrane is labeled with its length in µm, followed by an assigned membrane number $(1-4)$. All membranes seem to be stable and of decent optical quality.

Another important thing to note is, that the dissipation dilution formula is only valid for significant strain, as derived in Section 4.3. However, the resulting fit parameter for stress $\sigma = (4.5 \pm 0.2) \cdot 10^5$ Pa can be used to obtain the corresponding relative length change of the membrane using Eq. (4.12), resulting in a relative length change or shrinkage of only about $\varepsilon = 0.02\,\%$. This is also the reason why only Q-factors of up to $Q \approx 50$ were reached. A shrinkage of $\varepsilon = (2-12)\,\%$, which should be theoretically achievable with IP-S [35], using Eq. (4.12) and Eq. (4.16) again, would lead to Q-factors of the order of $Q \approx 1000$.
The resonance frequency is also strongly dependent on the membrane length. Here, the data was also fitted by using the formula for the resonance frequency of a stressed string Eq. (4.11). Similarly to the Q-factor, one can also obtain the fit parameter for stress $\sigma = (6.3 \pm 0.7) \cdot 10^5$ Pa, leading to a similar result for the relative length change of about $\varepsilon = 0.03\,\%$.
Another concern is that the strain in each individual membrane may not be uniform for a given scan speed, as assumed by these formulas, but instead could depend on the membrane length. This variation might occur due to the stochastic nature of the polymerization and printing process.
Nevertheless, progress has been made as the first increase of the Q-factor in our experiment was achieved. The assumption of the strain in the membranes increasing at higher scan speeds, also seems to be valid.

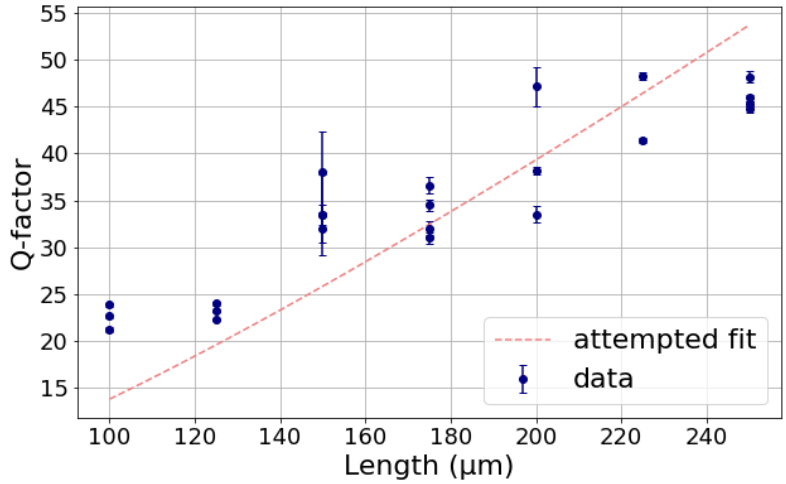

(a)

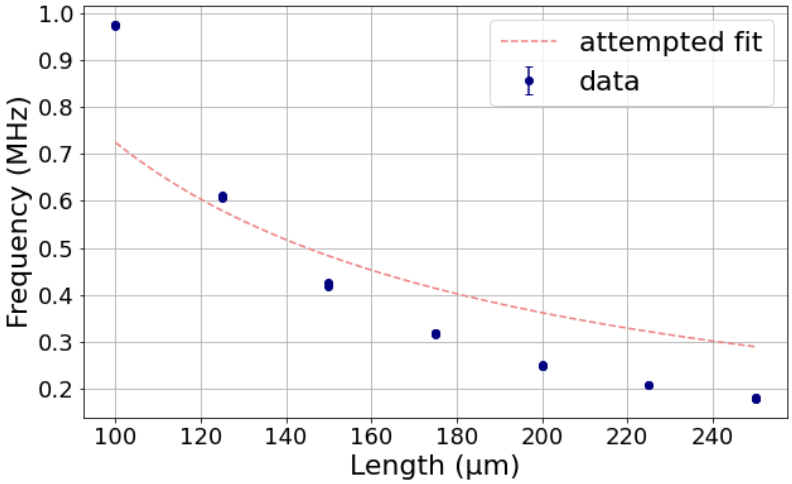

(b)

Figure 6.9: Plots of the dependence on the membrane length of both **(a)** the Q-factor and **(b)** the resonance frequency of the membranes. A clear dependence of the Q-factor on the length can be seen. However, the dissipation dilution factor model (Eq. (4.16)) is not fitting the data well. This is presumably due to the fact, that the strain, while present, is still low. This also shows in the increase of the Q-factor to "only" about $Q \approx 50$.

As already mentioned, for higher scan speeds of $ScSp > 10\,000\,\mu m\,s^{-1}$, many of the printed structures were unstable. The longer the membranes were, the higher was the rate of them breaking. Microscope images of selected printed membranes for a scan speed of $ScSp = 30\,000\,\mu m\,s^{-1}$ can be seen in Fig. 6.10. Here, many significant artefacts on the membrane surfaces can be seen. Images for other scan speeds can be found in Appendix A.2. For higher scan speeds, most of the membranes break entirely.
Measurements of the Q-factor for membranes written at higher scan speed have also been conducted, when possible. For some of the membranes, which looked promising in the microscope images, no sufficient optical signal for locking could be found. On the other hand, some membranes with large artefacts such as the first membrane with length $L = 225\,\mu m$, as shown in Fig. 6.10, could be measured successfully.
The successful measurements of the Q-factor Q and resonance frequency f_{res} for samples of stable membranes are shown in Table 6.1. The membranes, written with a scan speed of $ScSp = 20\,000\,\mu m\,s^{-1}$, had even lower Q-factors than membranes written at a scan speed of $ScSp = 10\,000\,\mu m\,s^{-1}$. This is likely due to the membranes cracking and breaking in general, which leads to a loss of strain. However, there were some membranes at scan speeds of $ScSp = 30\,000\,\mu m\,s^{-1}$ and $ScSp = 50\,000\,\mu m\,s^{-1}$, which even exceeded the previous record Q-factor with values close to $Q \approx 60$. These values were even reached for relatively short membranes with a length of $L = 150\,\mu m$, speaking for increased strain for higher scan speeds.

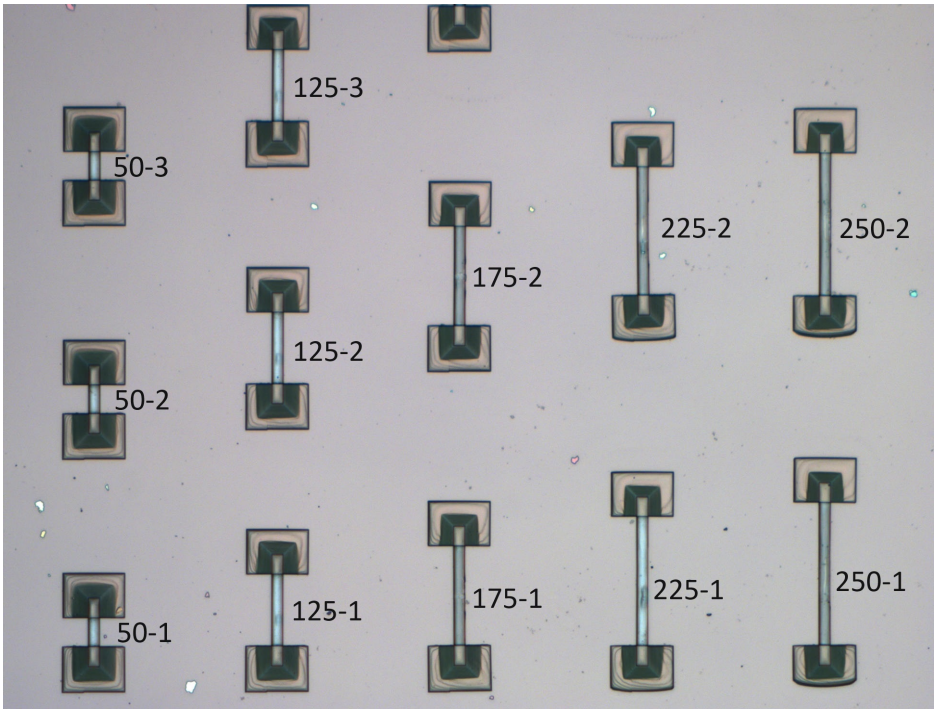

Figure 6.10: Microscope image of selected membranes written at a scan speed of $ScSp = 30\,000\,\mu m\,s^{-1}$. Each membrane is labeled with its length in µm, followed by an assigned membrane number $(1-4)$. Shorter membranes seem to have artefacts near the center of the membrane, while longer membranes seem to be cracked entirely.

However, these recorded Q-factors were exceptions among many entirely broken membranes. To possibly increase the consistency of the stability of these prints, thicker membranes were printed, as presented in the following in Section 6.3.

Table 6.1: Q-factors measured for thin galvo mode membranes with scan speeds of $ScSp > 10\,000\,\mu m\,s^{-1}$. Due to lack of data and higher inconsistencies for the high scan speeds, no data series dependent on length such as for $ScSp = 10\,000\,\mu m\,s^{-1}$ was recorded. Errors for the Q-factor and the resonance frequency f_{res} resulting from the fitting of errors of a Lorentzian to the signal, have been left out, as they are of an insignificant order of magnitude.

$ScSp$ ($\mu m\,s^{-1}$)	L (μm)	Membrane number	f_{res} (MHz)	approx. Q
20 000	225	3	0.23	31
20 000	225	4	0.24	31
20 000	250	1	0.2	34
20 000	250	2	0.2	32
20 000	250	3	0.2	38
30 000	200	4	0.25	52
30 000	225	1	0.21	57
30 000	225	2	0.18	38
30 000	250	1	0.15	40
30 000	250	2	0.15	42
50 000	150	1	0.38	59
50 000	150	2	0.38	50

6.3 Thick galvo mode membranes

In this section, the process of trying to improve the stability of membranes, written in the galvo mode at high scan speeds, is discussed. The measured Q-factors for thin membranes, as presented in Section 6.2, showed promising correlations between the scan speed and the induced strain in the membrane. To increase the stability for these membranes, to possibly make use of even higher scan speeds, the thickness of the membranes is significantly increased.
As thin membranes are desirable for dissipation dilution and for less optical losses, the printed thick membranes will be thinned by making use of oxygen-plasma ashing.

6.3.1 Finding parameters for printing stable membranes at high scan speeds

First tests with printing membranes with thicknesses of $h = (2 - 3)\,\mu\text{m}$ proved to produce stable membranes for lengths up to $L = 300\,\mu\text{m}$ for scan speeds of up to $ScSp = 50\,000\,\mu\text{m}\,\text{s}^{-1}$. This is the maximum length printable, without needing to use block splitting of the membrane, which is discussed in Section 5.1. The maximum laser power of $LP = 100\%$ also seemingly works best for very high scan speeds and is applied for the following prints. These prints, while stable, had lots of artefacts on the membrane surface and higher scan speeds were still not stable enough.
To take things a step further, membranes of thicknesses of $h = (5 - 10)\,\mu\text{m}$ were printed for scan speeds of $ScSp = (60\,000 - 90\,000)\,\mu\text{m}\,\text{s}^{-1}$. The resulting membranes were mostly stable for scan speeds of up to $ScSp = 60\,000\,\mu\text{m}\,\text{s}^{-1}$ for thicknesses of $h = 5\,\mu\text{m}$ and for all used scan speeds for thicknesses of $h = 10\,\mu\text{m}$. However, all membranes had large artefacts near their center. This can be seen for the example of membranes of a thickness of $h = 10\,\mu\text{m}$, written at a scan speed of $ScSp = 90.000\,\mu\text{m}\,\text{s}^{-1}$, in Fig. 6.11.

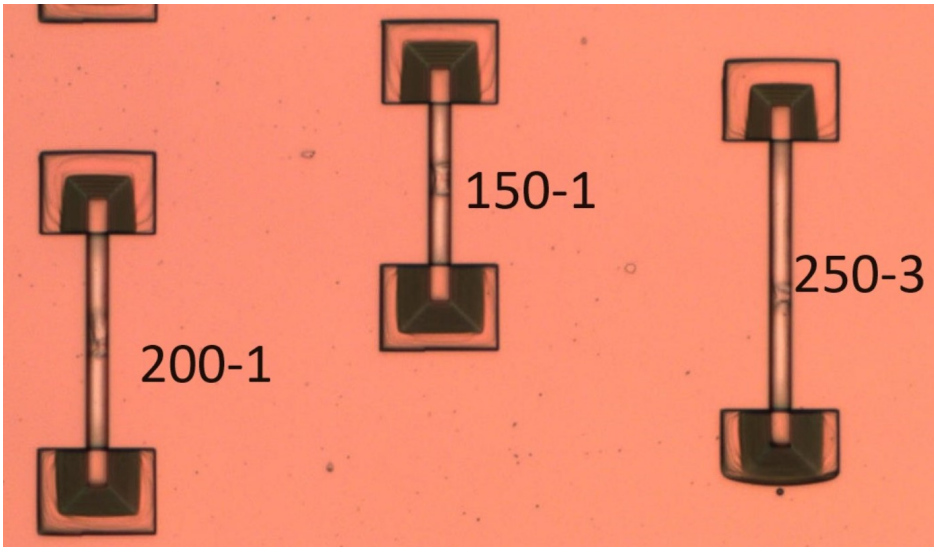

Figure 6.11: Microscope image of selected membranes with a thickness of $h = 5\,\mu\text{m}$ printed at a scan speed of $ScSp = 90.000\,\mu\text{m}\,\text{s}^{-1}$. None of the thick membranes collapsed. However, there are large artefacts near the center of the membranes.

It is unclear from looking at the microscope images whether these artefacts are only within the outer layers of the membranes or are present throughout. However, as the membranes did not fully collapse, there seems to be a connection of membrane layers, even at the center of the membrane. Overall, the surface looks uneven and might not be under tension anymore due to parts of the membrane snapping. This suspicion proved to be accurate when conducting a measurement of the Q-factors of selected membranes of the sample. All Q-factors for different scan speeds seemed to be limited to about $Q_{max} = 30$. The measurement process itself also proved to be difficult, as the optical quality of the membranes only allowed for very small coupling depths of up to $CD = 20\%$. Besides the increased membrane thickness, this can also be attributed to the surface roughness and artefacts of the samples.

6.3.2 Applying oxygen-plasma ashing on thick membranes

To potentially remove artefacts and loose layers from the outer surface of the thick membranes, printed at high scan speeds, oxygen-plasma ashing is applied. Here, a plasma source generates a highly reactive oxygen species. The oxygen combines with free chain ends of the polymer, forming ash, that is removed by a low-pressure vacuum pump, as illustrated in Fig. 6.12. The machine used is a plasma cleaning device (Zepto 119167 by Diener electronic). Apart from possibly removing loose membrane layers, the thickness is also decreased due to the isotropic ashing process, which is also beneficial for increasing the dissipation dilution factor.
As the machine was previously only used for surface polishing of polymer membranes in our experimental group [15], parameters for removing material on the order of micrometers had to be determined first. For this, the intensity and duration of the ashing process was adjusted iteratively, testing the process with previous test-prints. The “pumping down pressure” and “process pressure” were held constant at 0.2 mbar and 0.5 mbar respectively, while the duration and the relative intensity parameter were increased iteratively. The samples were inspected under a microscope after each iteration, until a clear change was visible.
Lower durations and intensities showed close to no visual effect. Eventually, an intensity of 90% was applied onto a sample with membranes with a thickness of $h = (2 - 3)\,\mu m$ and a cylindrical marker with a set thickness of $h = 4\,\mu m$ for 30 min. The result can be seen in Fig. 6.13. All of the membranes are fully decomposed, meaning that layers with a total thickness of at least $h = 3\,\mu m$ were removed. The cylinder is still present in parts. However, this only provides limited information, as the cylinder is directly attached to the mirror substrate from one side in contrast to the membranes. Consequently, the oxygen-plasma is only dissolving it from the top. However, it is unlikely that the

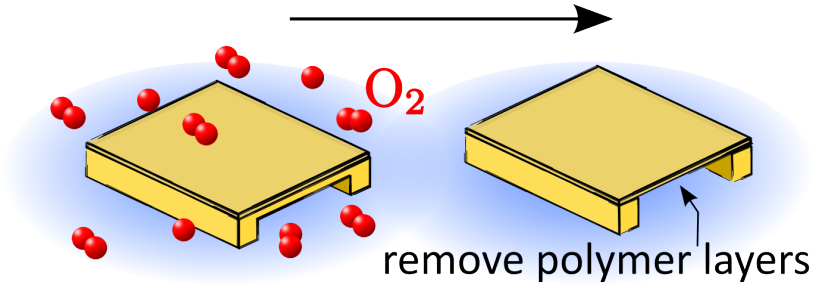

Figure 6.12: Schematic of the oxygen-plasma ashing process. A highly reactive oxygen species combines with the polymer of the membrane, forming ash. This way, multiple polymer layers can be removed.

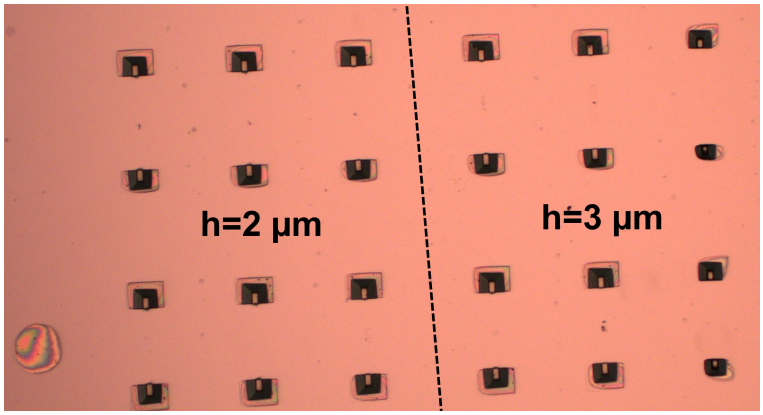

Figure 6.13: Test sample with initially $h = (2 - 3)$ µm thick membranes and a $h = 4$ µm thick cylinder, after applying oxygen-plasma ashing at an intensity of 90% for 30 min. All the membranes are fully removed, while a thin layer of the cylinder is still present.

exact same parameters fully remove a membrane with $h = 10$ µm thickness.
That is why the same parameters of an intensity of 90% for 30 min were then applied onto the sample with the membranes with a thickness of $h = (5 - 10)$ µm . Most of the structures with a thickness of $h = 5$ µm were completely removed by the oxygen-plasma treatment, as shown in Fig. 6.14. The shorter membranes, however, still seem intact. This could be due to the support structures shielding the membrane to a degree, as they are closer to the center of the membrane compared to for longer membranes. The longest membranes with a length of $L = (250 - 300)$ µm are close to fully removed, meaning they are likely thinned by about $\Delta h \approx 5$ µm. This is also consistent with previous testing.
The now thinned $h = 10$ membranes were closely inspected under a microscope again, as shown in Fig. 6.15 for a $L = 250$ µm and $L = 300$ µm long membrane printed at a scan speed of $ScSp = 60\,000\,\mu\mathrm{m\,s^{-1}}$. Unfortunately, the microscope images taken before the oxygen-plasma application, as seen in Fig. 6.11, were taken with a different microscope with a vastly different resolution. Therefore, it is difficult to make a direct comparison between the two. However, especially thanks to the dark field configuration of the microscope, the membrane surface after the ashing process can be seen in detail. The membrane surface does seem to be smoother overall. This strengthens the hypothesis that mostly the upper layers were loose, leading to damping of oscillations and therefore a lower Q-factor. However, all membranes still show cracks and other artefacts near the center, meaning that they likely lost a large portion of their strain.
To maximize the strain, one could try printing similar structures with a more coarse objective, like the 25x-objective. The larger voxels hopefully lead to less cracking of the membranes. A consequent oxygen-plasma treatment to reduce the thickness would still be possible. However, using an objective with less resolution will also result in worse optical properties but his could still be acceptable with the newly installed second fiber mirror, as discussed in Section 3.2. First testing for writing structures with the 25x-objective has been done. However, the required adjustment of all parameters would require more time to achieve significant results.

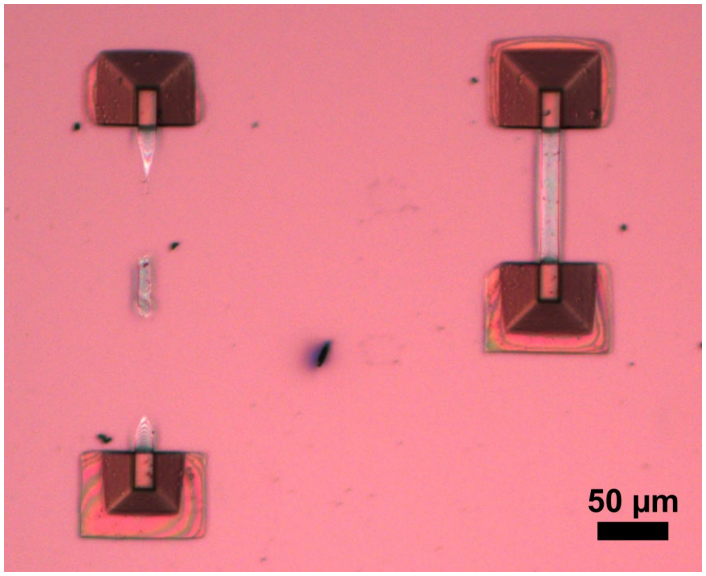

Figure 6.14: Membranes with initially $h = 5$ µm thickness after applying oxygen-plasma ashing at an intensity of 90 % for 30 min. All of the longer membranes are fully removed, while the shorter membranes are still intact.

6.3.3 Final measurements of oxygen-plasma treated membranes

To verify that the oxygen-plasma treatment does in fact increase the Q-factor by removing damping layers of the membrane, the measurement for multiple of the treated membranes at various scan speeds was attempted. The coupling depth when trying to measure the cavity signal over one of the treated membranes was generally very low ($CD < 20\,\%$). It has been shown previously [15] that oxygen plasma has the best effect on the optical quality, and therefore the surface roughness, when the surface roughness has already been sufficient even before the treatment. This does seem intuitive, as an uneven membrane surface prevents the plasma from removing layers evenly due to the varying surface area, meaning the poor surface roughness is not further improved.
The results for membranes, for which the Q-factor was successfully measured, can be found in Table 6.2.
The Q-factor increased relative to the limit of $Q_{max} = 30$ from before the treatment for all membranes. This means that the outer layers likely were damping the structures. The results are very inconsistent, due to the unpredictable damages to the membranes. However, multiple membranes reached a higher Q-factor than for the thin membranes, printed in Section 6.2. Two of the membranes even show a Q-factor of about $Q \approx 100$, which is an increase of a factor 5 relative to the intrinsic Q-factor of $Q \approx 20$.

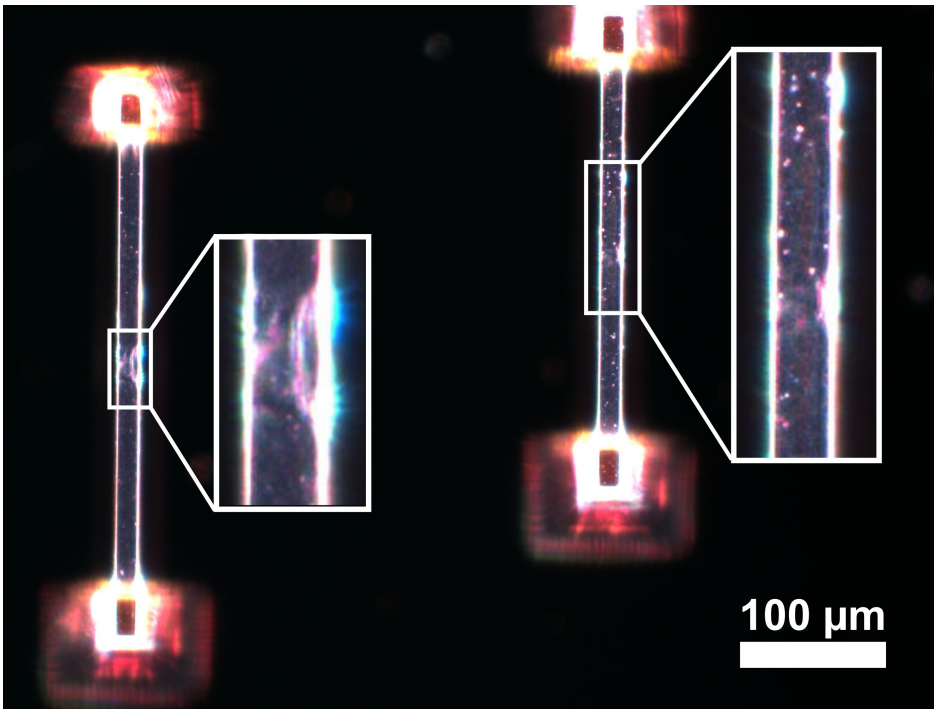

Figure 6.15: Dark-field microscope images of menbranes with lengths of $L = 250\,\mu m$ (number 4) and $L = 300\,\mu m$ (number 4), printed at a scan speed of $ScSp = 60\,000\,\mu m\,s^{-1}$. The center of all membranes still looks damaged to a degree. The surface, however, does seem smoother.

Table 6.2: Q-factors measured for thick galvo mode membranes with scan speeds of $ScSp > 60\,000\,\mu m\,s^{-1}$, after oxygen-plasma treatment. The Q-factor was only measurable for a few membranes due to the low coupling depth of the optical signal. Errors for the Q-factor and resonance frequency f_{res} resulting from the fitting of errors of a Lorentzian to the signal, have been left out, as they are of an insignificant order of magnitude.

$ScSp$ ($\mu m\,s^{-1}$)	L (μm)	Membrane number	f_{res} (MHz)	approx. Q
70 000	200	4	0.36	36
70 000	300	2	0.19	40
80 000	200	1	0.31	50
80 000	250	1	0.23	67
80 000	250	2	0.24	102
80 000	250	3	0.23	53
80 000	250	4	0.24	44
80 000	300	1	0.17	98
80 000	300	2	0.17	70
80 000	300	4	0.15	40
90 000	250	3	0.23	80
90 000	250	4	0.22	56

CHAPTER 7

Conclusion and Outlook

The goal of this thesis was to increase the mechanical Q-factor of the 3D direct laser written membranes used in our Fiber Cavity Optomechanics (FCO) experiment. The Q-factor of the membranes made out of IP-S resin, that was previously limited to $Q \approx 20$, has been successfully increased by a factor of 5 through the principle of dissipation dilution.
The optimization process, by adjusting the fabrication with the commercial Nanoscribe system, was started by writing structures similar to the previously fabricated membranes in our experiment. Here, the piezo mode with the 63x-objective, that provides the best possible optical quality due to its high resolution, was used to fabricate thin membranes with a thickness of about $h = 1\,\mu\text{m}$. No improvements were able to be made this way, as the piezo mode is strongly limited in the usable writing speed. Measurements showed that a higher writing speed leads to increased strain, which, in turn, increases the mechanical Q-factor.
That is why options with the faster galvo mode were explored. A new design for the membranes and their support structures was developed and writing parameters that can produce stable membranes were found. A measurement series was successfully conducted to demonstrate how the membrane length relates to the mechanical Q-factor due to dissipation dilution effects. Here, a Q-factor of $Q \approx 50$ was consistently reached.
To be able to increase the writing speed and, therefore, the strain in the fabricated membranes even further, membranes with a thickness up to $h = 10\,\mu\text{m}$ were printed. As loose layers on top of the membranes negatively impacted the Q-factor, an oxygen-plasma treatment was employed to remove these layers. This additionally decreased the thickness of the membranes by about 50 %. The treated membranes reached increased Q-factors of up to $Q \approx 100$.
Although this result is a great improvement, the Q-factor can still be further optimized in the future. While the loose layers of the thick membranes were successfully removed with the oxygen-plasma treatment, cracks in the structure were still visible. To achieve higher Q-factors, the membranes need to be generally more stable. One way of possibly achieving this, is by using the 25x-objective, which results in thicker voxel lines due to the objective's lower resolution, which could lead to more stability. This has been done successfully in another group [59]. However, due to their different field of application, the optical quality of the mechanical oscillator was neglected. While the optical quality will be lower for the 25x-objective, it is likely still sufficient. This is due to the new, second fiber mirror, that was installed into the experimental setup as another part of this thesis. The new fiber mirror has a higher transmission, leading to better impedance matching with lossier structures. First

testing with the 25x-objective has been done but one would require more time for optimizing the printing parameters.
A way of direct improvement would be putting the optomechanical system into a cryostat. This has been done with the previously manufactured membranes in the experiment to great success [15].
Other ways of improving the mechanical Q-factor, while maintaining the flexibility of 3D direct laser writing, is by using other resins like GP-Silica [61]. GP-Silica allows to print glass structures and offers higher intrinsic Q-factors, which is the limit for our system as of now. Furthermore, GP-Silica prints require an additional sintering step, involving controlled heating of the membrane up to 1 400 °C [62], to transform the original greenling print into glass. Since the cavity mirrors cannot withstand such high temperatures, this process is unsuitable for our drum-on-mirror integration. To address this, our group is currently working on an alternative to the sintering procedure with localized heating of the greenling using the CO_2 laser setup of the Bonn Fiber Lab.

Appendix

APPENDIX A

Appendix

A.1 Large dose test for piezo mode membranes

After the first dose test with structures written in the piezo mode, which was discussed in Section 5.2, another more elaborate dose test was carried out. In preparation for the length sweeps, shown in Section 6.1, the geometry of the membranes was adjusted to a length of $L = 100\,\mu m$ and width of $B = 25\,\mu m$. The design of the printing array, where both scan speed $ScSp$ and laser power LP are varied, can be seen in Fig. A.1. Compared to the first dose test, higher laser powers of $LP = (35-60)\,\%$ in 5 %-steps and higher scan speeds of $ScSp = (50-200)\,\mu m\,s^{-1}$ in $30\,\mu m\,s^{-1}$-steps were chosen. All membranes, except the ones with the lowest laser dose with scan speeds $ScSp \geq 30\,\mu m\,s^{-1}$ and lower laser powers $LP \leq 45\,\%$, were properly polymerized. For all of the other parameters, the inspection under the microscope showed stable membranes with decent looking surface quality.

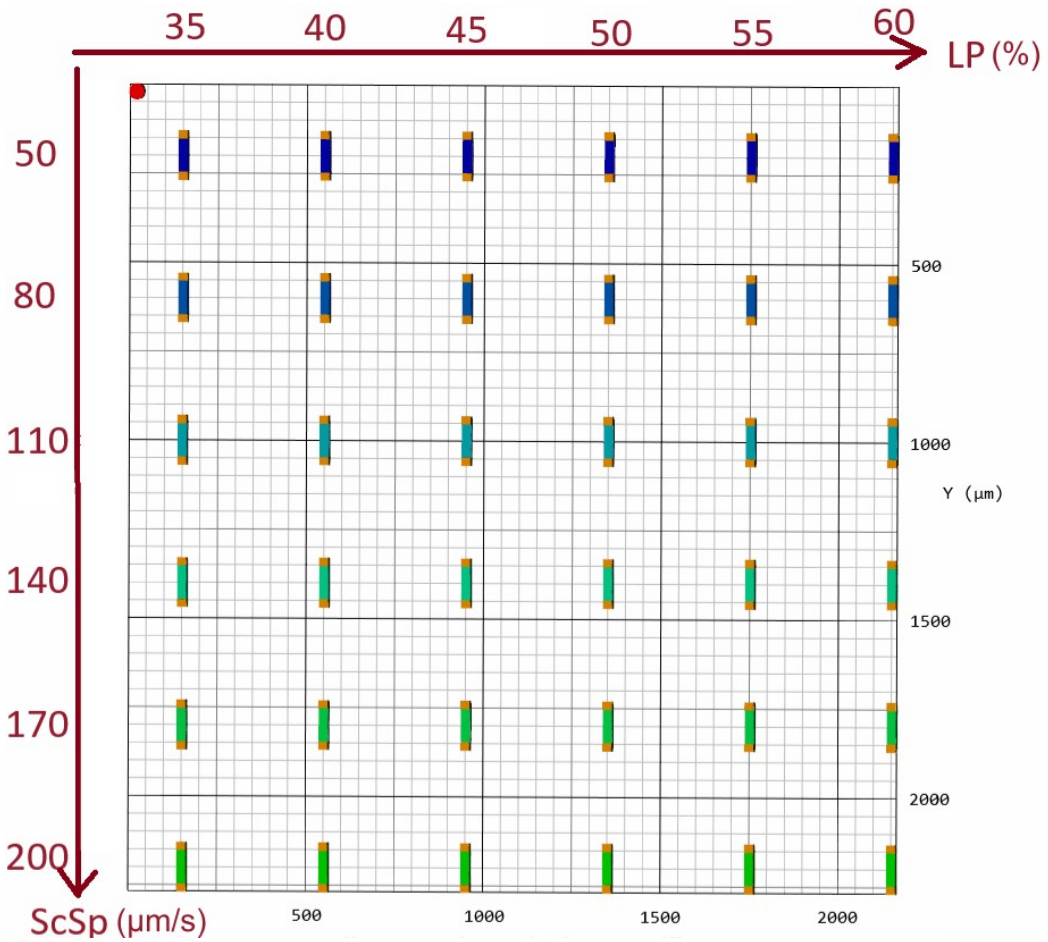

Figure A.1: Large follow-up dose test for membranes written in piezo mode. Each membrane has a length of $L = 100\,\mu m$ and width of $B = 25\,\mu m$. The parameters swept are the laser power $LP = (35 - 60)\%$ in 5 %-steps and scan speed $ScSp = (50 - 200)\,\mu m\,s^{-1}$ in $30\,\mu m\,s^{-1}$-steps.

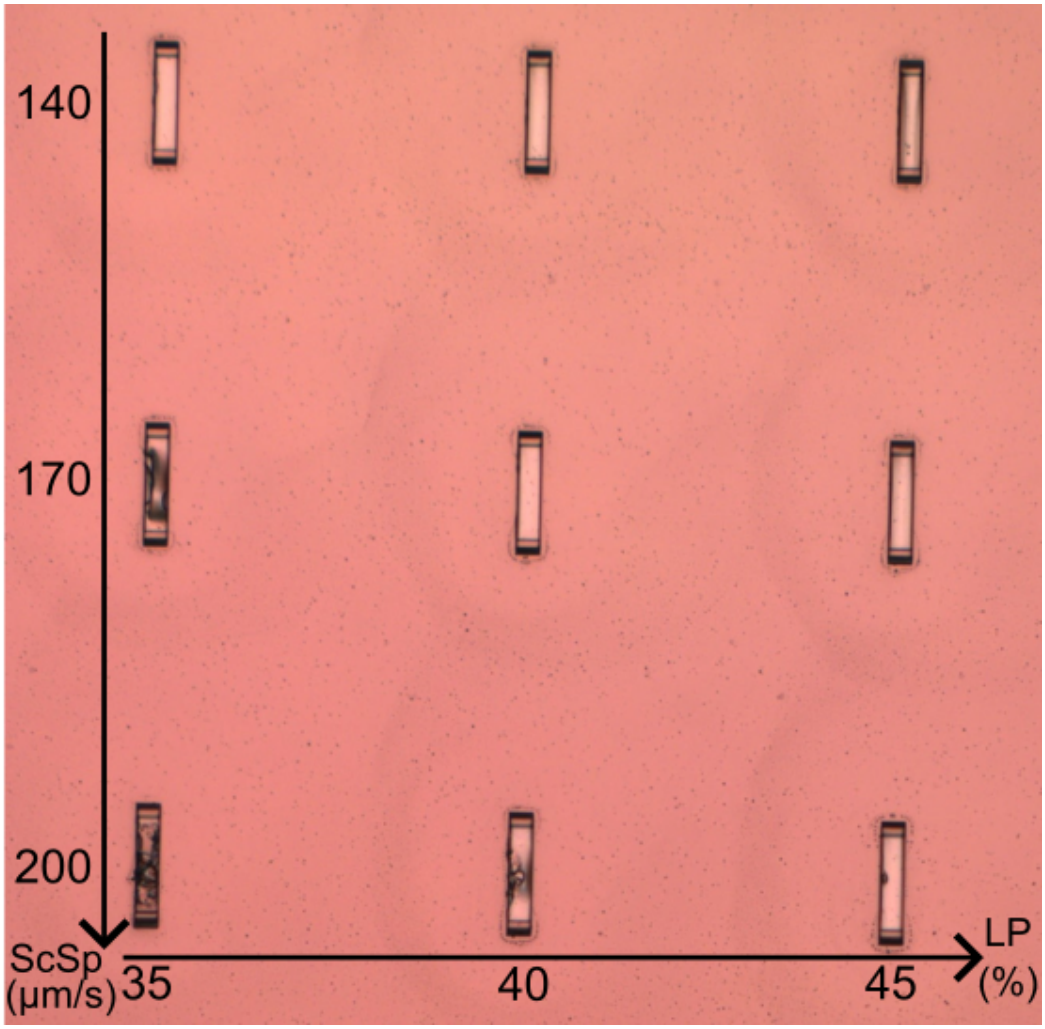

Figure A.2: Microscope image of a part of the membranes from the large dose test, written in the piezo mode. For the highest chosen scan speeds of $ScSp \geq 30\,\mu\mathrm{m\,s^{-1}}$ at lower laser powers of $LP \leq 45\,\%$, some of the membranes did not fully polymerize, as the laser dose was too low. All other parameters yielded stable results with decent surface quality.

A.2 Microscope images for thin membranes in galvo mode, higher scan speeds

Here, parts of the microscope images for thin membranes in galvo mode at various scan speeds can be seen in Fig. A.3, Fig. A.4, Fig. A.5 and Fig. A.6. Each membrane is labeled with its length in µm, followed by an assigned membrane number $(1-4)$.
For higher scan speeds, the general stability of the membranes is lower and longer membranes are not stable. Measurements of the Q-factors of some of these membranes can be found in Table 6.1 in Section 6.2.

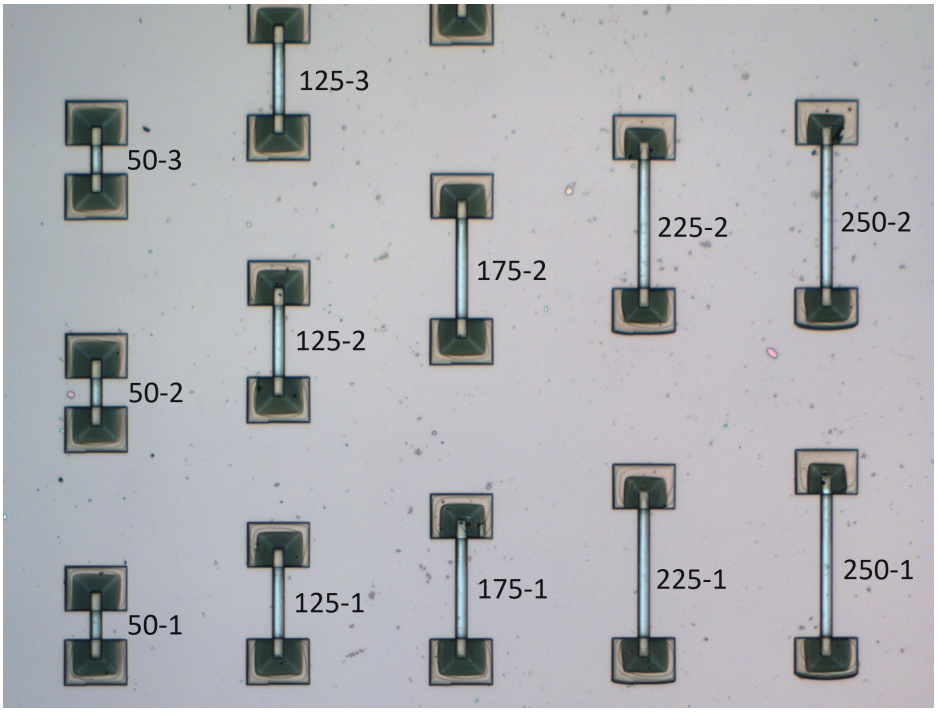

Figure A.3: Microscope image of selected membranes written at a scan speed of $ScSp = 20\,000\,\mu m\,s^{-1}$. Each membrane is labeled with its length in µm, followed by an assigned membrane number $(1-4)$

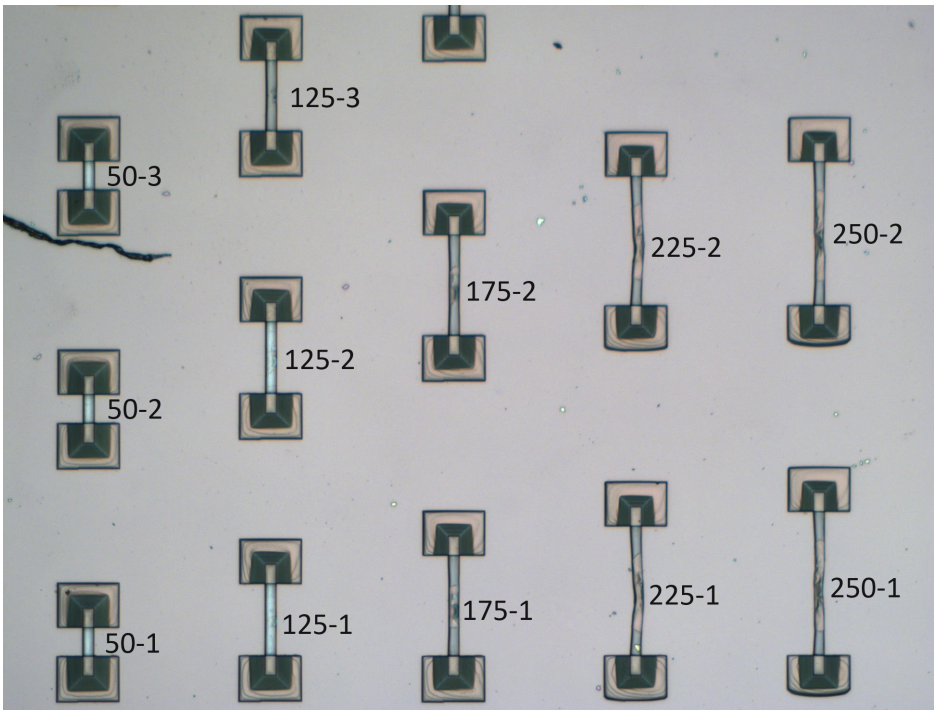

Figure A.4: Microscope image of selected membranes written at a scan speed of $ScSp = 40\,000\,\mu m\,s^{-1}$. Each membrane is labeled with its length in µm, followed by an assigned membrane number $(1-4)$

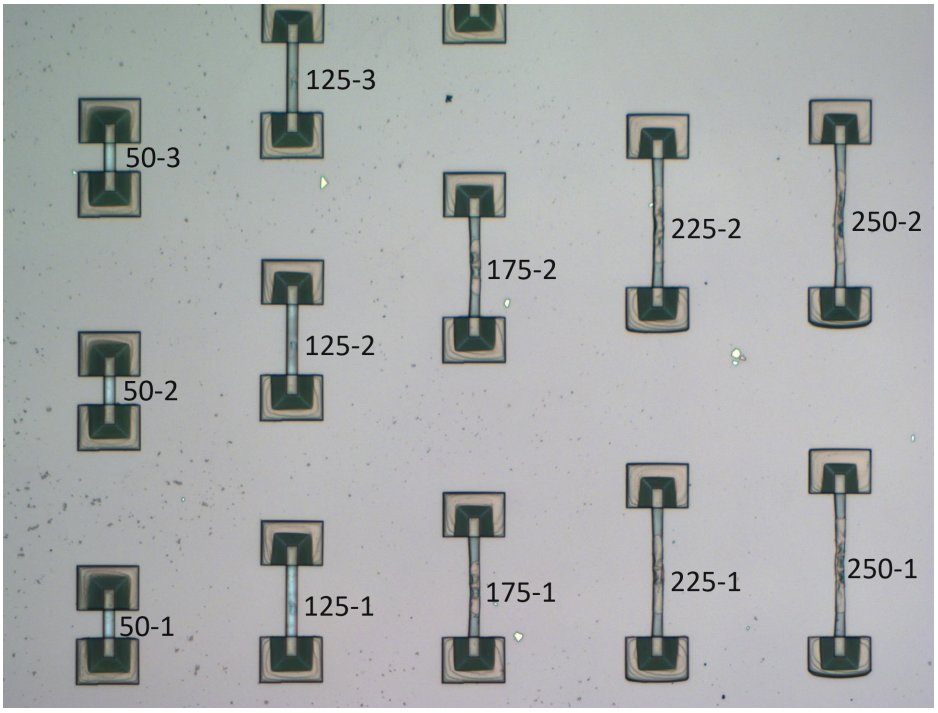

Figure A.5: Microscope image of selected membranes written at a scan speed of $ScSp = 50\,000\,\mu m\,s^{-1}$. Each membrane is labeled with its length in µm, followed by an assigned membrane number $(1-4)$

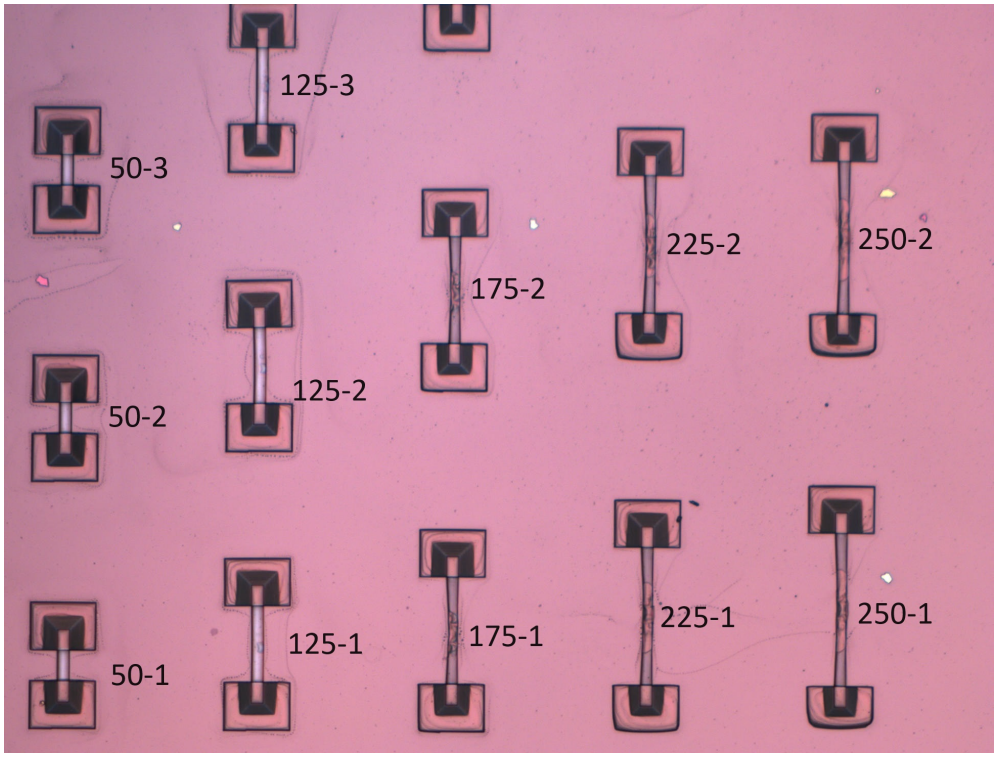

Figure A.6: Microscope image of selected membranes written at a scan speed of $ScSp = 20\,000\,\mu m\,s^{-1}$. Each membrane is labeled with its length in µm, followed by an assigned membrane number $(1-4)$

Bibliography

[1] S. Barzanjeh et al., *Optomechanics for quantum technologies*, Nature Physics **18** (2022) 15.

[2] J. Clarke, P. Neveu, K. E. Khosla, E. Verhagen and M. R. Vanner, *Cavity Quantum Optomechanical Nonlinearities and Position Measurement beyond the Breakdown of the Linearized Approximation*, Phys. Rev. Lett. **131** (5 2023) 053601.

[3] J. Chan et al., *Laser cooling of a nanomechanical oscillator into its quantum ground state*, Nature **478** (2011) 89.

[4] S. Gröblacher, K. Hammerer, M. R. Vanner and M. Aspelmeyer, *Observation of strong coupling between a micromechanical resonator and an optical cavity field*, Nature **460** (2009) 724.

[5] J. T. Hill, A. H. Safavi-Naeini, J. Chan and O. Painter, *Coherent optical wavelength conversion via cavity optomechanics*, Nature Communications **3** (2012) 1196.

[6] B.-B. Li, L. Ou, Y. Lei and Y.-C. Liu, Nanophotonics **10** (2021) 2799.

[7] J. D. Thompson et al., *Strong dispersive coupling of a high-finesse cavity to a micromechanical membrane*, Nature **452** (2008) 72.

[8] M. Aspelmeyer, T. J. Kippenberg and F. Marquardt, *Cavity optomechanics*, Rev. Mod. Phys. **86** (4 2014) 1391.

[9] K.-K. Ni et al., *Enhancement of Mechanical Q Factors by Optical Trapping*, Phys. Rev. Lett. **108** (21 2012) 214302.

[10] N. J. Engelsen, A. Beccari and T. J. Kippenberg, *Ultrahigh-quality-factor micro- and nanomechanical resonators using dissipation dilution*, Nature Nanotechnology **19** (2024) 725.

[11] B. Nair, A. Naesby and A. Dantan, *Optomechanical characterization of silicon nitride membrane arrays*, Opt. Lett. **42** (2017) 1341.

[12] L. Tenbrake, A. Faßbender, S. Hofferberth, S. Linden and H. Pfeifer, *Direct laser-written optomechanical membranes in fiber Fabry-Perot cavities*, Nature Communications **15** (2024) 209.

[13] C. Metzger, I. Favero, A. Ortlieb and K. Karrai, *Optical self cooling of a deformable Fabry-Perot cavity in the classical limit*, Phys. Rev. B **78** (3 2008) 035309.

[14] H. Pfeifer et al., *Achievements and perspectives of optical fiber Fabry–Perot cavities*, Applied Physics B **128** (2022).

[15] L. Tenbrake, *Fiber Cavity Optomechanics with Polymer Membranes*, MA thesis: Friedrich-Wilhelms University, 2021.

[16] D. Röser, *Fiber Fabry-Perot Cavities for Quantum Information and Spectroscopy*, 2019.

[17] R. Kitamura, L. Pilon and M. Jonasz, *Optical constants of silica glass from extreme ultraviolet to far infrared at near room temperature*, Appl. Opt. **46** (2007) 8118.

[18] D. Hunger, C. Deutsch, R. J. Barbour, R. J. Warburton and J. Reichel, *Laser micro-fabrication of concave, low-roughness features in silica*, AIP Advances **2** (2012) 012119, eprint: https://pubs.aip.org/aip/adv/article-pdf/doi/10.1063/1.3679721/12876463/012119_1_online.pdf.

[19] J. Gallego et al., *High-finesse fiber Fabry–Perot cavities: stabilization and mode matching analysis*, Applied Physics B **122** (2016) 47.

[20] R. E. Wagner and W. J. Tomlinson, *Coupling efficiency of optics in single-mode fiber components*, Appl. Opt. **21** (1982) 2671.

[21] Y. Yan et al., *Nanoliter-Scale Light–Matter Interaction in a Fiber-Tip Cavity Enables Sensitive Photothermal Gas Detection*, Laser & Photonics Reviews (2024), eprint: https://onlinelibrary.wiley.com/doi/pdf/10.1002/lpor.202400907.

[22] D. Hunger et al., *A fiber Fabry–Perot cavity with high finesse*, New Journal of Physics **12** (2010) 065038.

[23] D. Meschede, *Optics, Light and Lasers: The Practical Approach to Modern Aspects of Photonics and Laser Physics, First Edition (Physics Textbook)*, Wiley-VCH, 2004, ISBN: 3-527-40364-7.

[24] W. Demtröder, *Experimentalphysik 2*, Springer Spektrum Berlin, Heidelberg, 2018, ISBN: 978-3-662-55789-1.

[25] A. E. Siegman, *Lasers*, University Science Books, 1986, ISBN: 0-935702-11-3.

[26] N. Sharmin, A. Parsons, C. Rudd and I. Ahmed, *Effect of boron oxide addition on fibre drawing, mechanical properties and dissolution behaviour of phosphate-based glass fibres with fixed 40, 45 and 50 mol% P2O5*, Journal of biomaterials applications **29** (2014).

[27] F. Giefer, *Towards a Double Tip Vacuum Fiber Microscope*, BA thesis: Friedrich-Wilhelms University, 2022.

[28] TOPTICA, *General Error-Signal Generation Schemes*, URL: https://www.toptica.com/application-notes/phase-and-frequency-locking-of-diode-lasers/error-signal-generation/general-error-signal-generation-schemes#c15565 (visited on 07/11/2024).

[29] S. Schmid, L. G. Villanueva and M. L. Roukes, *Fundamentals of Nanomechanical Resonators*, Springer International Publishing, 2023, ISBN: 978-3-031-29628-4.

[30] D. Meschede, “Deformierbare Körper, Schwingungen und Wellen”, *Gerthsen Physik*, Berlin, Heidelberg: Springer Berlin Heidelberg, 2015 139, ISBN: 978-3-662-45977-5.

[31] H. M. Chu, *Air damping models for micro- and nano-mechanical beam resonators in molecular-flow regime*, Vacuum **126** (2016) 45.

[32] M. Bao, *Analysis and Design Principles of MEMS Devices*, First Edition, 2005, ISBN: 9780444516169.

[33] M. Bao, H. Yang, H. Yin and Y. Sun, *Energy transfer model for squeeze-film air damping in low vacuum*, Journal of Micromechanics and Microengineering **12** (2002) 341.

[34] J. A. Judge, D. M. Photiadis, J. F. Vignola, B. H. Houston and J. Jarzynski, *Attachment loss of micromechanical and nanomechanical resonators in the limits of thick and thin support structures*, Journal of Applied Physics **101** (2007), Cited by: 104.

[35] Nanoscribe, *IP-S*, URL: https://support.nanoscribe.com/hc/en-gb/articles/360001750353-IP-S (visited on 26/09/2024).

[36] R. A. Norte, J. P. Moura and S. Gröblacher, *Mechanical Resonators for Quantum Optomechanics Experiments at Room Temperature*, Phys. Rev. Lett. **116** (14 2016) 147202.

[37] P.-L. Yu et al., *A phononic bandgap shield for high-Q membrane microresonators*, Applied Physics Letters **104** (2014) 023510, eprint: https://pubs.aip.org/aip/apl/article-pdf/doi/10.1063/1.4862031/13545278/023510_1_online.pdf.

[38] M. Imboden and P. Mohanty, *Dissipation in nanoelectromechanical systems*, Physics Reports **534** (2014) 89, Dissipation in nano-electromechanical systems.

[39] J. Yang, T. Ono and M. Esashi, *Energy dissipation in submicrometer thick single-crystal silicon cantilevers*, Microelectromechanical Systems, Journal of **11** (2003) 775.

[40] C. Zener, *Internal Friction in Solids. I. Theory of Internal Friction in Reeds*, Phys. Rev. **52** (3 1937) 230.

[41] J. Brandrup, E. H. Immergut and E. A. Grulke, *Polymer Handbook*, John Wiley & Sons, 2003, ISBN: 978-0-471-47936-9.

[42] S. Kunze, R. Groll, B. Besser and J. Thöming, *Molecular diameters of rarefied gases*, Scientific Reports **12** (2022) 2057.

[43] J. Kestin and W. Leidenfrost, *An absolute determination of the viscosity of eleven gases over a range of pressures*, Physica **25** (1959) 1033.

[44] N. Khélifa, M. Lecollinet and M. Himbert, *Molar mass of dry air in mass metrology*, Measurement **40** (2007) 779, Precision Measurement of Force, Mass, and Torque.

[45] W. Demtröder, *Experimentalphysik 3*, Springer Spektrum Berlin, Heidelberg, 2016, ISBN: 978-3-662-49093-8.

[46] L. Sementilli, E. Romero and W. P. Bowen,
Nanomechanical Dissipation and Strain Engineering,
Advanced Functional Materials **32** (2022) 2105247,
eprint: https://onlinelibrary.wiley.com/doi/pdf/10.1002/adfm.202105247.

[47] S. A. Fedorov et al., *Generalized dissipation dilution in strained mechanical resonators*,
Phys. Rev. B **99** (5 2019) 054107.

[48] M. Singh and R. Singh, *Molecularly Imprinted Polymers (MIPs)*, Elsevier, 2023,
ISBN: 978-0-323-91925-8.

[49] Nanoscribe, *3D Printing using Two Photon Polymerization (2PP)*,
URL: https://support.nanoscribe.com/hc/en-gb/articles/360008908273-3D-Printing-using-Two-Photon-Polymerization-2PP (visited on 14/11/2024).

[50] Nanoscribe, *Photonic Professional GT+ Operating Manual*, 2021.

[51] J. Fischer and M. Wegener,
Three-dimensional optical laser lithography beyond the diffraction limit,
Laser & Photonics Reviews **7** (2013) 22,
eprint: https://onlinelibrary.wiley.com/doi/pdf/10.1002/lpor.201100046.

[52] G. de Miguel, G. Vicidomini, B. Harke and A. Diaspro,
"Chapter 8 - Linewidth and Writing Resolution",
Three-Dimensional Microfabrication Using Two-photon Polymerization, ed. by T. Baldacchini,
Micro and Nano Technologies, Oxford: William Andrew Publishing, 2016 190,
ISBN: 978-0-323-35321-2.

[53] S. Ruzin and H. Aaron, *1P vs 2P fluorescence imaging*,
URL: https://microscopy.berkeley.edu/2P/index.html (visited on 14/11/2024).

[54] Nanoscribe, *Printing with the 3D Microfabrication Solution Set Small Features (3D SF)*, URL:
https://support.nanoscribe.com/hc/en-gb/articles/360002424414-Printing-with-the-3D-Microfabrication-Solution-Set-Small-Features-3D-SF (visited on 17/11/2024).

[55] X. Zhou, Y. Hou and J. Lin, *A review on the processing accuracy of two-photon polymerization*,
AIP Advances **5** (2015) 030701, eprint: https://pubs.aip.org/aip/adv/article-pdf/doi/10.1063/1.4916886/12814087/030701_1_online.pdf.

[56] J. Purtov, A. Verch, P. Rogin and R. Hensel, *Improved development procedure to enhance the stability of microstructures created by two-photon polymerization*,
Microelectronic Engineering **194** (2018) 45.

[57] Nanoscribe, *Printing Modes*, URL: https://support.nanoscribe.com/hc/en-gb/articles/214082985-Printing-Modes (visited on 15/11/2024).

[58] P. F. Gao, G. Lei and C. Huang,
Dark-Field Microscopy: Recent Advances in Accurate Analysis and Emerging Applications,
Analytical Chemistry **93** (2021).

[59] J. de Winter, T. Manzaneque and M. K. Ghatkesar,
Damping of 3D-printed polymer microbeam resonators,
Journal of Micromechanics and Microengineering **34** (2023) 015004.

[60] A. Bauhofer and C. Daraio, *Neural networks for trajectory evaluation in direct laser writing*, The International Journal of Advanced Manufacturing Technology **107** (2020) 2563.

[61] Nanoscribe, *GP-Silica*, URL: https://support.nanoscribe.com/hc/en-gb/articles/360022237999-GP-Silica (visited on 19/11/2024).

[62] Nanoscribe, *GP-Silica*, URL: https://www.nanoscribe.com/en/products/gp-silica/ (visited on 19/11/2024).

Acknowledgements

Here, I briefly want to thank all of the people, who helped me during my thesis, personally as well as physics-wise.
Thank you, Sebastian Hofferberth, for the opportunity for doing my master thesis in your reseach group. I had a a great time for the entire last year.
I also want to thank Stefan Linden for being my second supervisor and making it possible to work on a great project with the Nanoscribe.
A great thank you to everyone from the FCO. Lukas, thanks for the great support and the fun time spent together in the office as well as the lab. Also, thank you Florian and Jana for making the office a joyful place at all times. Additional thanks to Benedikt and Johanna. Even though, we have spent less time together, it was still great with you two.
Also, a gernal thank you to everyone from the NQO. Be it former or present members. Everyone is among the nicest people I have ever met.
Special thanks to my friends, family and in particular Julia for all the support and motivation throughout the year.